



# Dynamic responses of ultralight all-metallic honeycomb sandwich panels under fully confined blast loading

Xue Li <sup>a,b</sup>, Rui Kang <sup>a,b</sup>, Cong Li <sup>c</sup>, Zhiyang Zhang <sup>a,b</sup>, Zhenyu Zhao <sup>a,b,\*</sup>, Tian Jian Lu <sup>a,b,\*</sup>

<sup>a</sup> State Key Laboratory of Mechanics and Control of Mechanical Structures, Nanjing University of Aeronautics and Astronautics, Nanjing 210016, PR China

<sup>b</sup> MIIT Key Laboratory of Multifunctional Lightweight Materials and Structures, Nanjing University of Aeronautics and Astronautics, Nanjing 210016, PR China

<sup>c</sup> Marine Design & Research Institute of China, Shanghai 200011, PR China

## ARTICLE INFO

### Keywords:

Sandwich panel  
Honeycomb core  
Fully confined blast  
Dynamic response

## ABSTRACT

Fatal threats of fully confined blasts to surface battleships must be minimized to avoid catastrophic failure such as ship sinking. In the present study, for enhanced blast resistance, ultralight all-metallic sandwich panels with square honeycomb cores are proposed as an alternative to traditional metallic plates for ship construction. A combined experimental and numerical approach is employed to investigate the dynamic responses of fully-clamped sandwich panel subjected to fully confined blast loading and compare its blast resistance to that of its monolithic counterpart having equal mass. To explore the underlying physical mechanisms, finite element simulations with the Coupled Eulerian-Lagrangian (CEL) approach are performed. The simulation results are validated against experimental measurements for both sandwich and monolithic target plates, with good agreement achieved. It is demonstrated that, with the pressure versus time history on target plate featured by multiple reflected overpressures and a long-duration quasi-static phase with considerably lower pressure amplitude, the proposed sandwich panel exhibits a considerably higher blast resistance than its monolithic counterpart of equal areal density placed at the same standoff distance, due mainly to its consumption of impact energy via global out-of-plane bending, in-plane stretching, and localized core crushing. Results of this study are helpful for designing novel lightweight protection structures with enhanced blast resistance for ship construction.

## 1. Introduction

Advanced missiles with time-delay or smart fuses pose fatal threats to major surface battleships, which can detonate the critical chambers (e.g., ammunition compartment) after penetrating the ship hull, causing catastrophic failure such as ship sinking (due to, say, missile strike like that recently experienced by the flagship of Russian Black Sea Fleet, the Moskva Guided Missile Cruiser). Such internal blasts are commonly referred to as confined explosions, which is a main category of air blast loads based on confined shock wave propagation [1]. Relative to unconfined blasts (e.g., explosions in free air), confined explosions are much less well studied, for blast loadings on a target can be considerably aggravated by confinement, thus difficult to characterize [2]. It has been established that, with identical charge mass, internal blasts in confined space are significantly more intensive than unconfined ones, as energy concentration of the former is generally hundreds of times higher than that generated by the latter [3–6].

The intricate process associated with internal blasts, from explosive detonation to the formation and propagation of shock waves that ultimately interact with the structure (target), had been investigated by several earlier studies [2,7–9]. The results show that, due to confinement effects, the structure as a whole is subjected to an initial high-pressure shock wave and subsequent pulses with multiple reflections /superpositions that are complicated to describe, whereas its corner (connected to adjacent structures) is subjected to convergent shock wave. Eventually, the structure experiences a gas pressure that is dependent upon the volume and venting area of the confined space as well as the characteristics of explosives. Such devastating confined blast loadings may lead to severe damage to ship structures, causing even structural collapse and sinking of the ship. It is therefore of great significance to understand and characterize the dynamic response of a target structure subjected to fully confined blast loading, so as to achieve improved design for enhanced blast resistance.

Under fully confined blast, the dynamic response of a target is related

\* Corresponding authors at: State Key Laboratory of Mechanics and Control of Mechanical Structures, Nanjing University of Aeronautics and Astronautics, Nanjing 210016, PR China.

E-mail addresses: [sufengxing@foxmail.com](mailto:sufengxing@foxmail.com) (Z. Zhao), [tjlu@nuaa.edu.cn](mailto:tjlu@nuaa.edu.cn) (T. Jian Lu).

<https://doi.org/10.1016/j.compstruct.2023.116791>

Received 14 September 2022; Received in revised form 4 January 2023; Accepted 10 February 2023

Available online 15 February 2023

0263-8223/© 2023 Elsevier Ltd. All rights reserved.

to key influencing factors of both the blast chamber and explosive charge. For the former, the scaled-down blast chamber model is usually employed to determine the blast load and the response characteristics of a geometrically similar full-size target structure. Varying the size of the chamber according to the law of geometrical similarity for confined blast loading at the same scaled distance revealed that the larger the volume, the higher the reflected pressures [10–13]. On the other hand, relatively few studies reported the significant effect of chamber shape, e. g., rectangular, cuboidal, cylindrical, and spherical chambers, on target responses [2,14–16]. A series of internal blast tests were conducted in cuboidal steel containers to quantify the effect of explosive mass on permanent deformations of target structures [1]. As expected, the permanent deflection increased with increasing charge mass. Unexpectedly, however, increasing the standoff distance of charge resulted in monotonically increasing permanent displacement of either a square plate or stiffened plate [17–19], which contradicts the results of well-known free-air blast tests and is mainly attributed to blast wave attenuation [20]. In addition, the blast loading arising from detonation of a large-mass explosive charge is sensitive to its shape. In modern standards for blast-resistant design, spherical charge is commonly assumed, such as the UFC-3–340-02 (2008) [21], which gave a significantly lower prediction of deformation and damage responses of target structure than an axially/radially oriented cylindrical-shaped charge [9]. The same conclusion was reached in numerical simulation studies on seamless steel pipes subjected to internal explosive loadings from a centrally located cylindrical explosive charge and its equivalent spherical charge [14]. Recently, a combined experimental and numerical study was conducted to investigate the dynamic response of a stiffened steel plate subjected to the detonation of cylindrical TNT charge [22]. It was revealed that plate thickness plays a more significant role in the permanent deformation of the plate relative to the size of stiffeners attached to the plate. Further, in a recent study [23], the dynamic responses of metallic plates containing different types of preformed holes were studied to mimic the effects of perforation by fragments in combined fragment-blast loading.

Previous studies of confined blasts focused largely on conventional structures, such as mild steel plates and stiffened steel plates widely adopted for ship construction. In the present study, to alleviate the damaging effect of confined blast loading, ultralight all-metallic sandwich panels comprising thin face sheets and low-density cellular cores are envisioned, for they exhibit superior blast/impact resistance relative to traditional monolithic/stiffened plates of equal mass in unconfined blast loading [24–27]. The distinct advantages of such blast-resistant sandwich constructions are mainly attributed to three aspects [24,28–30]: (1) shock load mitigation by fluid–structure interaction (FSI) between the fluid-transported shock wave and the impacted face sheet of sandwich panel; (2) large plastic deformation and preeminent kinetic energy-absorbing capacity of cellular core; (3) high bending resistance of sandwich construction. When subjected to free air explosions, however, the smaller permanent deflection of a sandwich panel than its equivalent monolithic plate is dominated by the last two aspects, since the FSI effect in air shock loading is insignificant [25,30]. Ideally, for superior blast resistance, the sandwich panel with cellular core requires a strong, simultaneous stretching resistance core that keeps its face sheets separated to maintain high structural bending resistance.

Among numerous core topologies that have been exploited hitherto, the honeycomb with straight webs is favored due to its high crushing strength, along with low relative density (or, equivalently, high porosity) and excellent in-plane stretching resistance under unconfined air-blast loadings [24,31,32]. While a wide variety of cell geometries exist for honeycombs, the square and hexagonal honeycombs are commonly adopted for sandwich constructions against unconfined air-blast loadings. Early works [28,33–35] found that square-honeycomb core sandwich structures have a higher shock resistance than sandwiches having other core topologies (e.g., corrugated core and pyramidal core) of equal mass from the point of the permanent transverse

deflection. For sandwich panels made with hexagonal honeycomb cores, the effects of face sheet and core configuration on their dynamic responses under blast loading have been systematically investigated [36–38]. Recently, for applications in automotive, aerospace and marine industries, honeycomb-core sandwich constructions made with polymers [39,40] and fiber-reinforced composite materials [41,42] other than traditional metallic materials have attracted much attention.

Single and multiobjective design optimizations with a variety of heuristic algorithms have been carried out to further enhance the mechanical performances and weight efficiency of honeycomb sandwich structures. For instance, recent studies on numerical strategies for optimal design of honeycomb sandwiches can be found in [43] for minimized dynamic deflection or acceleration under blast loading, in [44] for maximized specific energy absorption under high-velocity impact, in [45] for minimal weight design and [46] for maximized transverse deflection and core crushing strain under impact loading, and in [47] for optimized structural weight and crashworthiness. Nonetheless, existing studies of sandwich structures have targeted mainly unconfined air blasts, with little attention paid to their performance under fully confined blasts typically encountered in modern surface battle-ships. This is the key motivation behind the current study. Therefore, with particular focus placed upon exploring whether sandwich design offers significant structural advantage over monolithic plates of equal mass, this study combines experimental measurements and finite element (FE) simulations to investigate the dynamic performance of honeycomb sandwich panels subjected to fully confined blast loading.

The paper is organized as follows. Section 2 presents the topological geometry and fabrication route of honeycomb sandwich panels. Section 3 outlines the experimental arrangements and objectives, while details of FE simulation for fully confined explosion based on the Coupled-Eulerian-Lagrangian (CEL) method are presented in Section 4. In Section 5, in addition to presenting experimental and numerical results, the dynamic responses of honeycomb sandwich panel under fully confined blast loading are quantitatively analyzed and compared with those of its monolithic counterpart. The study provides further insights for exploiting ultralight all-metallic sandwich structures with high resistance to fully confined explosions.

## 2. Morphology and fabrication of all-metallic honeycomb sandwich panels

### 2.1. Morphology of sandwich panels

L907A low-alloy marine steel (density  $\rho_f = 7850 \text{ kg/m}^3$  and yield strength 470 MPa), independently developed in China, has been extensively employed in marine industry for ship construction and hence is selected as the material make of the reference monolithic target plate as well as the front face sheet of the proposed sandwich panel. The thickness of the front face is fixed at  $t_f = 3 \text{ mm}$  in the current study. Fundamental mechanical properties of L907A steel have been characterized systematically in our earlier study [48,49]: the use of L907A as the front face sheet of sandwich construction allows the energy of impact loading to be dissipated via plastic bending and ductile stretching. The square honeycomb core and the back face are both fabricated from 316L stainless steel of thickness 1.5 mm and density  $7900 \text{ kg/m}^3$ , mainly for two reasons. Firstly, the shipbuilding steel L907A is relatively thick, having a minimum thickness of 3 mm according to the standard GJB 6055–2007. Honeycomb core fabricated with 3 mm thick L907A steel sheet is too strong for fully confined blast testing considered in the present study. Secondly, with high elongation ( $>50 \%$ ), excellent welding performance (especially for joining dissimilar materials at relatively low cost [50]), good corrosion resistance and stability in gaseous and aqueous environments, 316L stainless steel has also been widely exploited in marine industry. Thus, under fully confined blast loading, while the 316L honeycomb core takes full advantage of plastic crushing for energy absorption, the 316L back face sheet prevents the



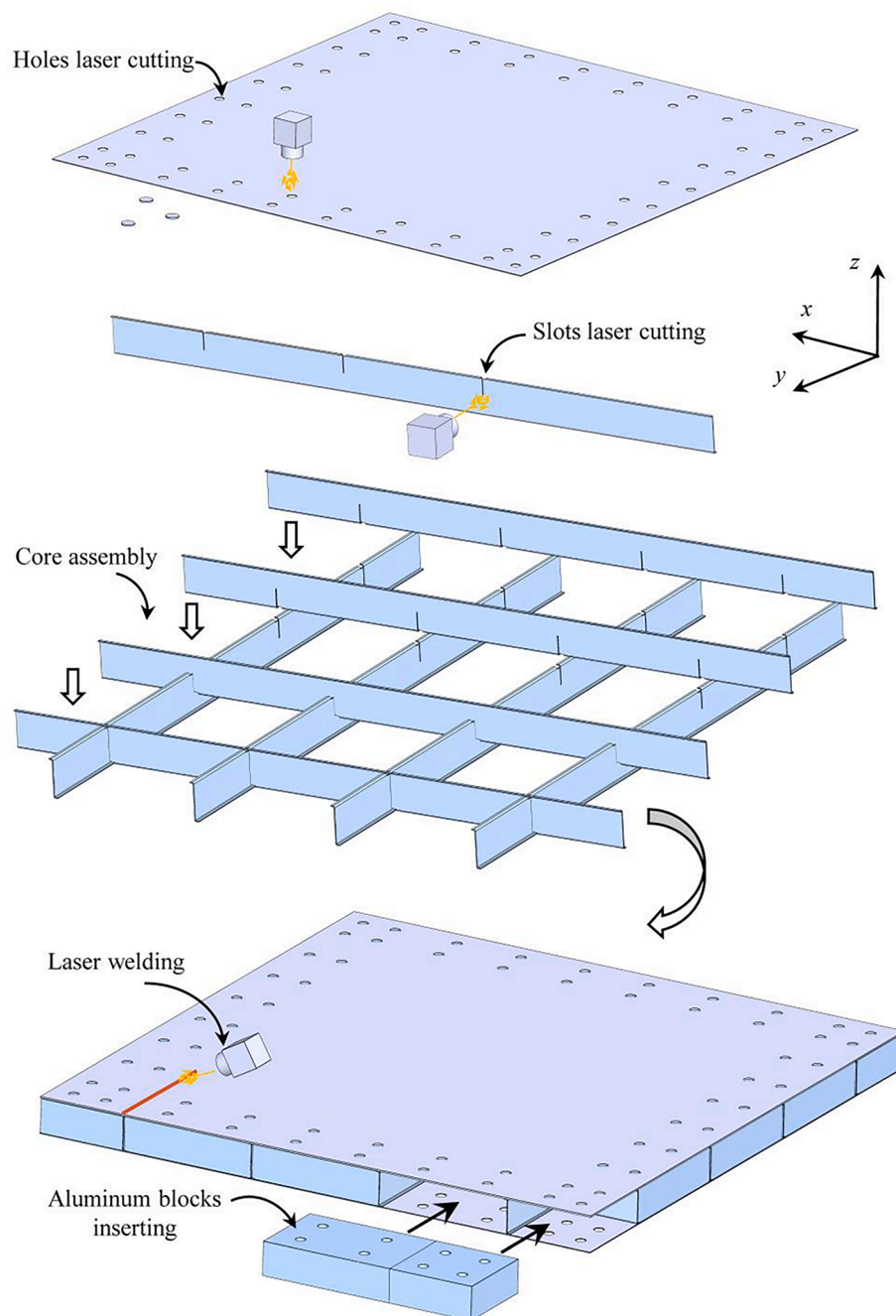


Fig. 2. Fabrication process of sandwich panel with flange-enhanced square honeycomb core.

sheets.

### 3. Fully confined blast tests

Fully confined blast tests carried out on edge-clamped sandwich panels with square honeycomb cores and their monolithic counterparts are summarized in Table 1, together with details of test specimens and blast conditions (e.g., mass, diameter and location of TNT charge). With spherical charges adopted, the tests consist of two groups: Group M and Group S. In Group M, monolithic target plates (specimens A and B; Table 1) are installed on both ends of the blast chamber. In Group S, a sandwich panel (specimen A) is mounted on one end of the chamber while its monolithic counterpart (specimen B) is mounted on the other end. Internal pressures recorded during each confined blast test and permanent mid-span displacements of target plates measured after the

test is completed are employed to determine the accuracy and fidelity of subsequent 3D FE simulations.

Fully confined blast tests are performed in a purposely designed and fabricated rectangular blast chamber that has an effective length of 2000 mm, a width of 900 mm, and a height of 900 mm. As shown in Fig. 3a, the left and right ends of the chamber are left unclosed before test specimens are mounted using M22 bolts. The entire chamber, made from 30 mm thick Q345B steel sheet, is designed according to the Pressure Vessel Preparation Standard GB.150–2011 of China. The chamber is welded using a multi-pass GTAW/SMAW/SAW process, followed by post-weld heat treatment to relieve residual thermal stresses and improve weldment properties. Likely defects in the welded joints are assessed with radiography testing, following procedures detailed in the NB/T47013-2015. The chamber is subsequently reinforced with T-shaped steel stiffeners, angled irons, and staggered steel ribs along both

**Table 1**  
Summary of confined blast tests.

Test	Schematic illustration	Specimens	Charge mass (kg)	Charge diameter (mm)	Standoff distance (m)
M-1		A: Monolithic plate 316L (1.5 mm) B: Monolithic plate 316L (1.5 mm)	0.27	73.5	R1 = 1 R2 = 1
M-2		A: Monolithic plate L907A (3 mm) B: Monolithic plate L907A (10 mm)	0.75	98.7	R1 = 1 R2 = 1
M-3		A: Monolithic plate L907A (3 mm) B: Monolithic plate L907A (3 mm)	1	108.4	R1 = 1 R2 = 1
S-1		A: Honeycomb core sandwich B: Monolithic plate L907A (10 mm)	0.75	98.7	R1 = 1 R2 = 1
S-2		A: Honeycomb core sandwich B: Monolithic plate L907A (3 mm)	1	108.4	R1 = 1 R2 = 1

longitudinal and transversal directions; Fig. 3a. This ensures the chamber has sufficiently strong resistance to internal explosive pressure, thus enabling confined blast tests to be carried out repeatedly.

During each test, the bottom of the as-fabricated rectangular blast chamber is fixed upon ground fixtures, also made of Q345B steel, via M16 bolts; Fig. 3a. The edge-clamped test specimens, either sandwich panel or its monolithic counterpart or both, and the chamber together create a fully confined space, with an effective 900 × 900 mm specimen area exposed to internal blast loading. Fig. 3b displays the assembled blast chamber with test specimens mounted on both of its ends, ready for fully confined blast test. The placing of TNT explosive charge is achieved via a handhole located at the top of chamber and a hook welded to the

inner wall of the chamber; Fig. 3c. The handhole is closed after the placing, and remains closed till the blast test is completed. The horizontal standoff distance between the charge and target can be varied as desired using hooks welded to top chamber wall. It should be pointed out that, to allow for unconfined blast tests, a functioning venting hole with a diameter of 250 mm is introduced to one of the sidewalls of rectangular chamber, as shown in Fig. 3a. Throughout the present tests, however, this venting hole is closed to ensure fully confined blast loading.

Two piezoresistive transducers placed at positions P1 and P2 and one piezoelectric transducer placed at position P3 are used for internal pressure measurements. The gauges (pressure transducers) are placed on

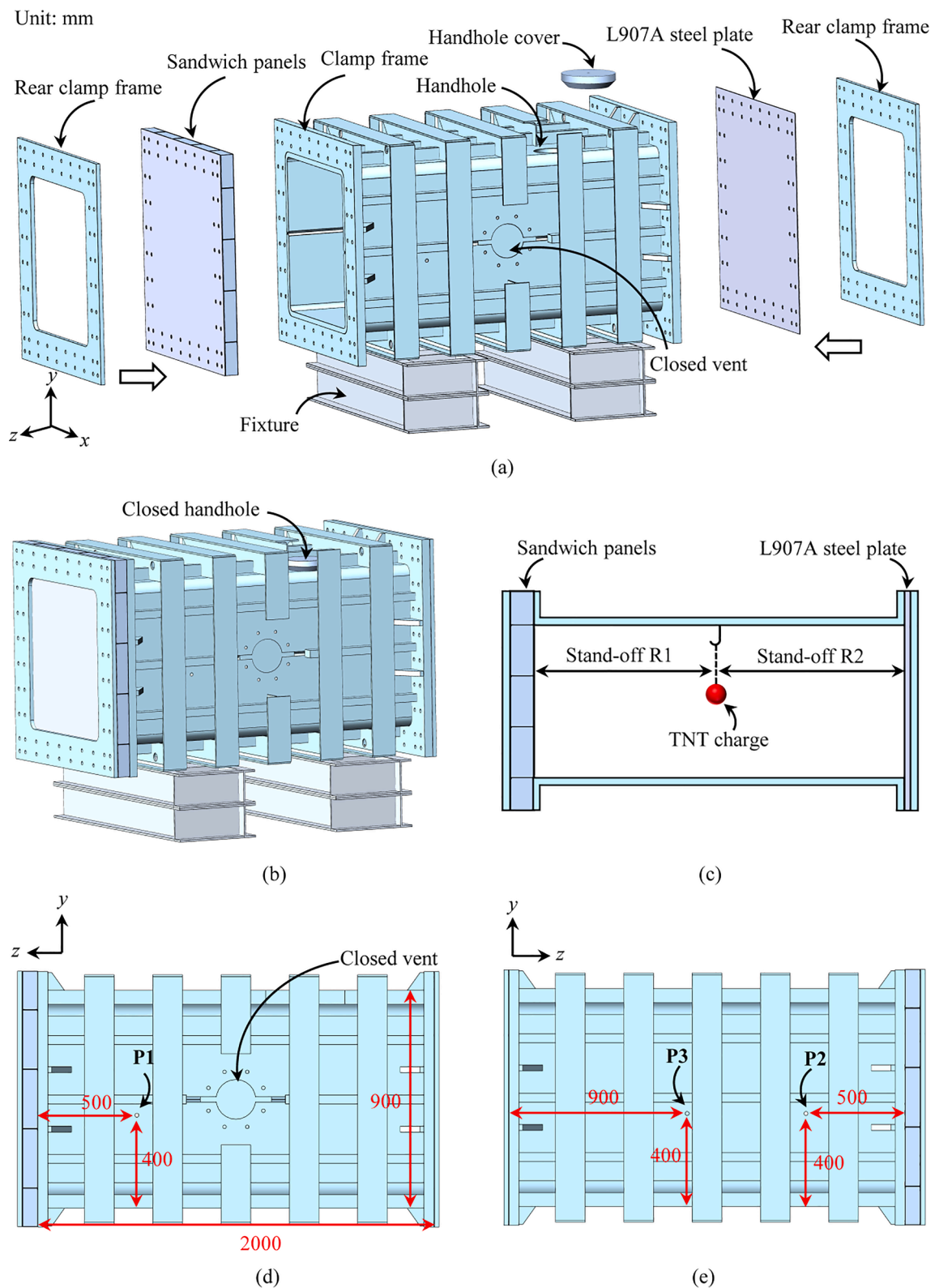


Fig. 3. (a) Schematic of purposely designed and fabricated rectangular chamber for confined blast test (e.g., Test S-1 detailed in Table 1), with a handhole on its top wall for placing TNT charge, (b) assembled chamber with edge-clamped test specimens and ground fixture, (c) cross-sectional view of standoff distances, R1 and R2, between spherical TNT charge and target plates (e.g., sandwich panel and its monolithic counterpart), (d) position of pressure transducer P1 on front side wall, and (e) positions of pressure transducers P2 and P3 on back side wall.

the front/back side walls of blast chamber (rather than the top wall) to keep away from the handhole, as shown in Fig. 3d and 3e. Gauges P1 and P2 (Keller PA-33X, KELLER HCW) with a working range of 0 ~ 30 MPa and measurement accuracy of  $\pm 0.01\%$  are used to measure quasi-static pressures on chamber walls: the two pressure transducers are positioned opposite to each other, one on the front side wall (Fig. 3d) and the other on the back side wall (Fig. 3e). To measure the reflected overpressure, gauge P3 (KD2000, Kedong Co., Ltd) with a working range of 0 ~ 60 MPa and an accuracy of  $\pm 0.5\%$  mounted on the back side wall is used. The three pressure transducers, P1, P2 and P3, have the same sampling frequency of 1000 kHz. For each blast test, pressure signal data are recorded via a data acquisition system. Upon completing each blast test, permanent mid-span deflections and deformation profiles of sandwich/monolithic specimens are measured.

#### 4. Finite element simulations

In addition to field tests, numerical modeling is necessary to explore

physical mechanisms and provide in-depth details of pressure wave interactions during fully confined explosion. In this study, three-dimensional (3D) finite element (FE) calculations are performed using the commercially available FE code ABAQUS/Explicit. This section presents details of the modeling procedure, including blast chamber and test specimen geometries, material constitutive models, boundary conditions, and mesh sensitivity studies, with relevant parameters carefully chosen to replicate experimental conditions.

##### 4.1. Finite element model

Fig. 4a displays a 3D FE model of representative blast test (i.e., Test S-1 of Table 1), which is consisted of air, blast chamber, specimens (i.e., sandwich panel and its monolithic counterpart in Test S-1) placed at both ends of chamber, spherical explosive charge (TNT), clamp frames, and bolts. Due to symmetry, only one-quarter of the FE model is presented. For the sandwich panel, identical flanges of core web as those in test specimens are considered, as shown in the enlarged view of

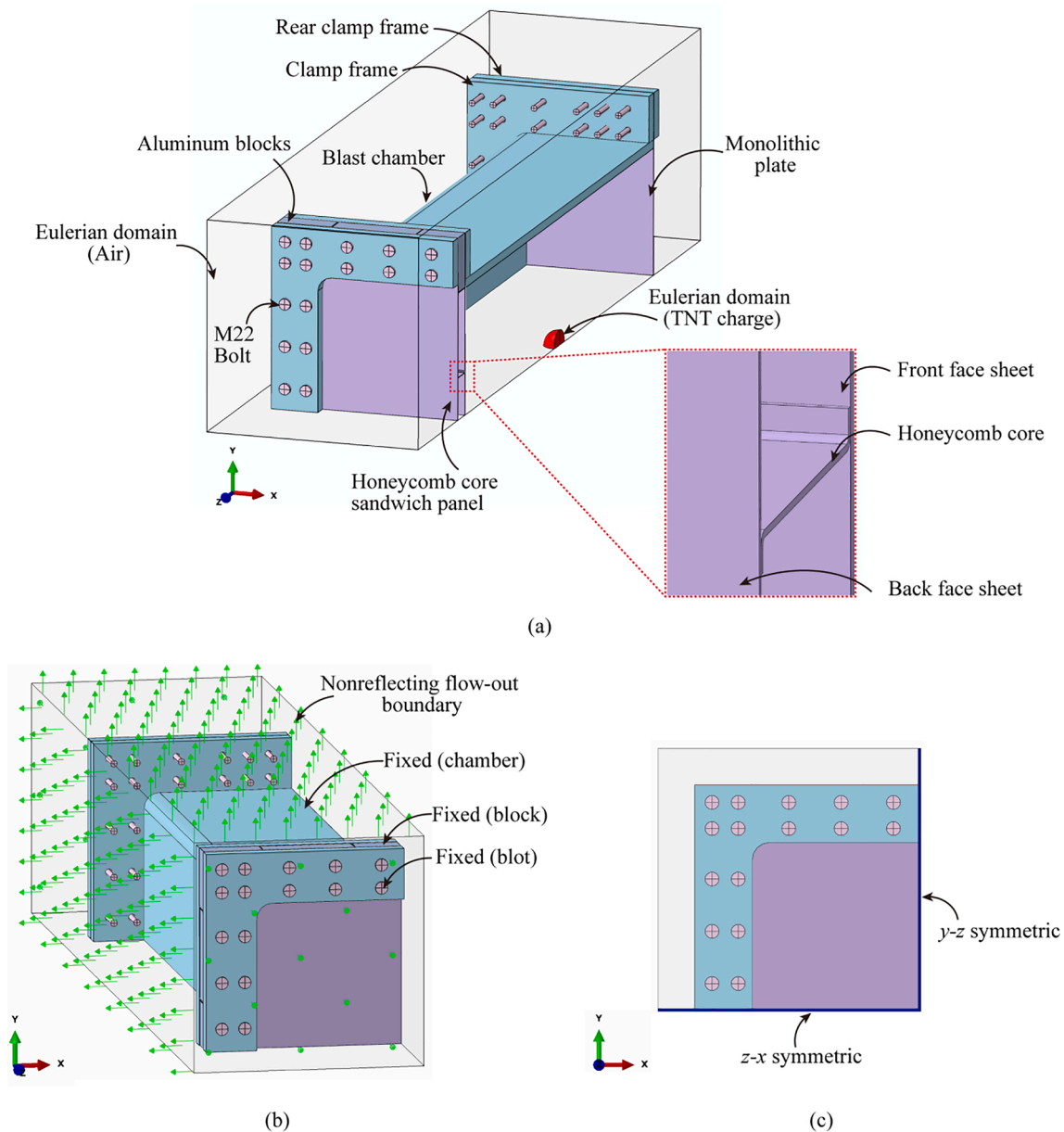


Fig. 4. (a) Schematic of 3D one-quarter FE model with one honeycomb sandwich panel and one monolithic plate mounted to the ends of blast chamber as target plates, and (b)-(c) boundary and symmetric conditions of the one-quarter model.

sandwich in Fig. 4a. In addition, aluminum blocks are inserted into the edges of sandwich panel for the purpose of clamping. In the present simulations, the rectangular chamber with clamp frames, the aluminum blocks, and the bolts are all fully fixed in space.

Structural dynamic responses of target plates subjected to fully confined explosion are calculated using the Coupled-Eulerian-Lagrangian (CEL) method [51,52]. This method enables capturing fluid-structure interaction between the Eulerian parts (i.e., the air and explosive charge) and the Lagrangian parts (i.e., the structural components), which has been shown to be effective in the simulation of impulsive blast involving extreme structural deformation. In this study, the Eulerian parts fixed in space are meshed using eight-node reduced integration (EC3D8R) hexahedral elements, while the Lagrangian C3D8R elements are adopted to mesh the structural components. The Eulerian domain has a dimension of  $3000 \times 750 \times 750$  mm, separated into two parts (Fig. 4a), i.e., the explosive domain and the air domain, with the former providing explosive material and the latter supplying air material. Eulerian materials can flow through Eulerian elements that do not deform, for the nodes are thoroughly fixed in space. Moreover, they can interact with Lagrangian elements via Eulerian-Lagrangian contact to get dynamic structural responses. It is emphasized that the volume covered by Eulerian parts should be larger than that of Lagrangian parts, thus giving enough space for Eulerian materials to move and deform. During the simulation, the Eulerian Volume Fraction (EVF) is tracked for each Eulerian element, which represents the ratio of Eulerian material inside an element to the volume of that element [51,52]. If an element is void without any material, its EVF is zero; if the EVF is unity, the element is completely filled with Eulerian material, which might be air, explosive, or both.

Nonreflecting flow-out boundary conditions are set to the Eulerian domain on each side to simulate an unbounded domain (Fig. 4b), such that Eulerian material can flow out of the Eulerian domain. If any Eulerian material moves outside the Eulerian mesh, it is lost from the simulation and corresponding decreases in total mass and energy would occur [53]. On the other hand, symmetric boundary constraints are set for the symmetry planes (Fig. 4c). The chamber, clamp frames, aluminum blocks, and bolts are fully clamped to represent the actual boundary conditions used in blast tests. Symmetrical boundary conditions are applied to the target plates on both sides of the chamber.

The general contact property models and defaults in ABAQUS are applied to the Eulerian-Lagrangian contact as well as the contact between each target plate and the clamping structural parts (i.e., clamp frames, aluminum blocks, and bolts). For the sandwich panel, the flanged honeycomb cores and the face sheets are perfectly bonded together using a tie-contact option. As post-test inspection showed that the welded joints are almost intact (Fig. 9), tie-contact is considered feasible in the present FE simulation.

The chamber is modeled as a rigid body in the FE model, for two reasons. Firstly, the chamber is not only constructed with sufficiently thick steel plates but also reinforced with T-shaped steel stiffeners, angled irons, and staggered steel ribs along both longitudinal and transversal directions. As a result, during the present blast tests, no visible deformation of chamber walls is observed. Secondly, as the 3D finite element model is relatively large, modeling the chamber as a rigid body reduces considerably the computational cost.

To analyze the characteristics of numerically simulated internal pressure loading generated during confined blast, three points on chamber walls are selected, consistent with positions P1, P2 and P3 in experimental setup (shown in Fig. 3d and 3e). For each test, upon detonation of spherical TNT charge, the FE simulation captures at least the first five milliseconds of structural response.

#### 4.2. Material constitutive models

Consider first the constitutive modeling of Eulerian materials. The standard JWL (Jones-Wilkins-Lee) equation of the state (EOS) model has

been widely employed to model the detonation of explosive, which expresses the pressure generated by chemical energy in an explosive as a function of its volume and energy [54], namely:

$$p_T = A \left( 1 - \frac{\omega}{R_1 \nu} \right) e^{-R_1 \nu} + B \left( 1 - \frac{\omega}{R_2 \nu} \right) e^{-R_2 \nu} + \frac{\omega E}{\nu} \quad (4)$$

where  $A$ ,  $B$ ,  $R_1$ ,  $R_2$  and  $\omega$  are the constants, to be determined from experiments, and  $p_T$ ,  $\nu$  and  $E$  are the pressure, relative volume, and internal energy per unit volume of the explosive, respectively.

The JWL EOS is based on the assumption of thermal isolation, since temperature is not defined in the model. In addition, the model is not suitable for explosives having low detonation velocities, for the reaction zone at the detonation front is thick compared with high detonation velocity explosives [55]. For the TNT explosive used in the present study, relevant material properties and parameters appearing in the JWL EOS model are listed in Table 2.

The air is modeled based on the assumption that it can be treated as an ideal gas [53,56], yielding:

$$p_A = (\gamma - 1)\rho_0 e - p_0 \gamma = c_p / c_v \quad (5)$$

where  $\rho_0$  is the initial density of the air;  $p_0$  is the atmospheric pressure;  $c_p$  and  $c_v$  are the specific heat at constant pressure and volume, respectively, whose ratio is defined as  $\gamma$  ( $\gamma=1.4$ ); and  $e$  is the internal energy per unit reference volume. This model is applicable for adiabatic analysis with constant specific heat and has much to commend for its simplicity and ease of computation. The values of relevant parameters appearing in the model are listed in Table 2.

Dynamic responses of the structural steels used in the current study, namely, marine steel L907A, AISI 316L stainless steel, and 40Cr steel (material makes of bolts for clamping) are described using constitutive models of plasticity and fracture initiation. Firstly, L907A is assumed to be isotropic such that it yields according to the von Mises-type yield criterion; correspondingly, the mixed Swift-Voce isotropic strain hardening model coupled with strain rate and temperature-dependent terms has been calibrated with great accuracy in our previous investigation [48]. On the other hand, ductile fracture is assumed to occur with the onset of plastic flow localization. The Hosford-Coulomb (H-C) fracture model is used to predict ductile fracture initiation of L907A steel, which is developed based on plasticity model in conjunction with a separate fracture model. It has been demonstrated that fracture initiation in L907A under various stress states, strain rates, and temperatures can be well described using the proposed plasticity and ductile fracture models [48]. The models have been implemented into ABAQUS via user-defined material subroutines, with calibrated model parameters listed in Table 3. For completeness of the current study, relevant formulas are summarized below.

The von Mises-type equivalent yield stress  $\sigma_y$  of the plasticity model is expressed as [48]:

$$\sigma_y = [\alpha A(\bar{\epsilon}_p + \epsilon_0)^n + (1 - \alpha)(k_0 + Q(1 - e^{-\beta \bar{\epsilon}_p}))] (1 + C \ln \dot{\epsilon}^*) [1 - (T^*)^m] \quad (6)$$

where the first and second terms in the first bracket can be re-expressed using the Swift-Voce hardening law, as:

$$k_s = A(\bar{\epsilon}_p + \epsilon_0)^n, k_v = k_0 + Q(1 - e^{-\beta \bar{\epsilon}_p}) \quad (7)$$

where  $\dot{\epsilon}^* = \dot{\epsilon}_p / \dot{\epsilon}_0$  and  $T^* = (T - T_r) / (T_m - T_r)$ . The Swift-Voce hardening law is a linear combination of the power-law ( $k_s$ ) and exponential-law ( $k_v$ ) types, where  $(A, \epsilon_0, n)$  are material parameters of the Swift model,  $(k_0, Q, \beta)$  are coefficients of the Voce equation, and  $\alpha$  is a weighting factor. The logarithmic term in Eq. (6), consisting of parameter  $C$  and reference strain rate  $\dot{\epsilon}_0$ , represents the effect of strain rate hardening. The thermal softening term includes the exponent  $m$ , the reference temperature  $T_r$ , and the melting temperature  $T_m$ .

**Table 2**  
Constitutive models parameters of Eulerian materials - TNT explosive [54] and air [53,56] - for numerical simulation.

Material	EOS parameters input data in ABAQUS							
	$\rho$ (kg/m <sup>3</sup> )	A (Pa)	B (Pa)	$R_1$ (-)	$R_2$ (-)	$\omega$ (-)	$E$ (J/m <sup>3</sup> )	$\nu$ (m/s)
TNT	1630	$3.71 \times 10^{11}$	$3.23 \times 10^9$	4.15	0.95	0.3	$7.0 \times 10^9$	6900
Air	$\rho_0$ (kg/m <sup>3</sup> ) 1.225	$p_0$ (Pa) 101,957	$R$ (J/kg-K) 287	$c_v$ (J/kg-K) 717.6		$c_p$ (J/kg-K) 1004.6		

\* Specific gas constant  $R = c_p - c_v$ .

**Table 3**  
Material properties and calibrated material parameters for L907A marine steel [48].

Material parameter	Notation	Numerical value
Young's modulus	$E$ (GPa)	202
Poisson ratio	$\nu$	0.3
Density	$\rho$ (kg/m <sup>3</sup> )	7850
Plateau stress	$\sigma_0$ (MPa)	472.68
Plateau strain	$\bar{\epsilon}_{plat}$	0.02097
Swift hardening constants	$A$ (MPa)	909.29
	$\epsilon_0$	0.0182
	$n$	0.1992
Voce hardening constants	$k_0$ (MPa)	382.96
	$Q$ (MPa)	259.44
	$\beta$	16.832
	$\alpha$	0.75
Weighting factor	$C$	0.0293
Strain rate-related constant	$\dot{\epsilon}_0$	0.001
Reference strain rate	$m$	0.840
Thermal softening constant	$T_r$ (K)	293
Reference temperature	$T_m$ (K)	1700
Melting temperature	$a$	1.811
Parameter related to Lode angle	$b_0$	1.0358
Controlling the overall magnitude	$c$	0.0019
Parameter related to stress triaxiality	$\gamma$	-0.0144
Parameter related to strain rate	$d$	3.973
Parameter related to temperature		

Consider next the ductile fracture initiation model for L907A [48]. The phenomenological H-C model of fracture initiation defines, at the instant of fracture, the equivalent plastic strain  $\bar{\epsilon}_f$  as a function of the stress triaxiality  $\eta$  and the Lode angle parameter  $\bar{\theta}$ , as:

$$\bar{\epsilon}_f(\eta, \bar{\theta}) = b(1 + c)^{\frac{1}{n}} \left( \left\{ \frac{1}{2} ((f_1 - f_2)^a + (f_2 - f_3)^a + (f_1 - f_3)^a) \right\}^{\frac{1}{a}} + c(2\eta + f_1 + f_3) \right)^{-\frac{1}{n}} (1 + dT^*) \quad (8)$$

where the Lode angle parameter-dependent trigonometric formulas are:

$$f_1(\bar{\theta}) = \frac{2}{3} \cos \left[ \frac{\pi}{6} (1 - \bar{\theta}) \right], f_2(\bar{\theta}) = \frac{2}{3} \cos \left[ \frac{\pi}{6} (3 + \bar{\theta}) \right], f_3(\bar{\theta}) = -\frac{2}{3} \cos \left[ \frac{\pi}{6} (1 + \bar{\theta}) \right] \quad (9)$$

and

$$b = \begin{cases} b_0 & \text{if } \dot{\bar{\epsilon}}_p < \dot{\epsilon}_0 \\ b_0(1 + \gamma \ln \dot{\bar{\epsilon}}^*) & \text{if } \dot{\bar{\epsilon}}_p \geq \dot{\epsilon}_0 \end{cases}, \dot{\bar{\epsilon}}^* = \dot{\bar{\epsilon}}_p / \dot{\epsilon}_0, T^* = (T - T_r) / (T_m - T_r) \quad (10)$$

The constants of the H-C model include: the Hosford exponent related to the Lode angle  $a$ , the multiplier  $b$ , the coefficient related to stress triaxiality  $c$ , the constant  $\eta$ , and the constants  $(\gamma, d)$  appearing in the strain rate and temperature-dependent terms.

As for the AISI 316L stainless steel, it is assumed that the empirical Johnson-Cook (J-C) model [57] can be employed to characterize its flow stress and fracture behavior, which considers the effects of strain, strain rate, and temperature. For the plasticity model, the equivalent yield stress  $\sigma_y$  is expressed as:

$$\sigma_y = \left( A + B\bar{\epsilon}_p^n \right) (1 + C \ln \dot{\bar{\epsilon}}^*) [1 - (T^*)^m] \quad (11)$$

where the strain rate and temperature-dependent terms have the same form as Eq. (6). The constants  $A, B$ , and  $n$  are material parameters of the hardening model, which is only a power-law type in comparison with the Swift-Voce model. In the current study, the three parameters are obtained by fitting the expression  $(A + B\bar{\epsilon}_p^n)$  with the measured average true stress versus true strain curve of AISI 316L. Uniaxial true stress versus strain curves of AISI 316L are obtained by performing quasi-static tensile tests using three nominally identical specimens (Fig. 5a), each conducted at an engineering strain rate of  $1 \times 10^{-3} \text{ s}^{-1}$  using an MTS testing machine (CMT5105) at room temperature, with a longitudinal extensometer employed for deformation measurement. As the true stress versus true strain curves displayed in Fig. 5b are almost identical, the average of measurement results is taken as representative of material response. Fig. 5c further plots error bars (standard deviations) for true stresses measured at selected true strains, which indicate that the present test data are highly repeatable. In addition, the values of strain rate and temperature parameters  $C$  and  $m$  appearing in Eq. (11) are taken from existing studies [58], as listed in Table 4.

To characterize the ductile fracture of AISI 316L, the J-C fracture model [59] considers the effects of stress triaxiality, strain rate and temperature on failure strain but is independent of the Lode angle,

resulting in:

$$\bar{\epsilon}_f = D_1 + D_2 \exp(D_3 \eta) [1 + D_4 \ln \dot{\bar{\epsilon}}^*] (1 + D_5 T^{*m}) \quad (12)$$

where  $D_1$  is a material constant,  $D_2$  and  $D_3$  are the stress triaxiality-dependent parameters, while the coefficients  $D_4$  and  $D_5$  are related to strain rate and temperature, respectively. Based on the published data [60], the parameters of the J-C fracture model for AISI 316L are listed in Table 4. Finally, for the bolt material 40Cr, the Johnson-Cook material model is also used and the corresponding fitted parameters, taken from reference [61], are presented in Table 4.

#### 4.3. Mesh convergence

To obtain a proper mesh size for FE simulations, mesh convergence analysis for typical cases, i.e., Test M-3 and Test S-2 listed in Table 1, is carried out to investigate the sensitivity of simulated mid-span

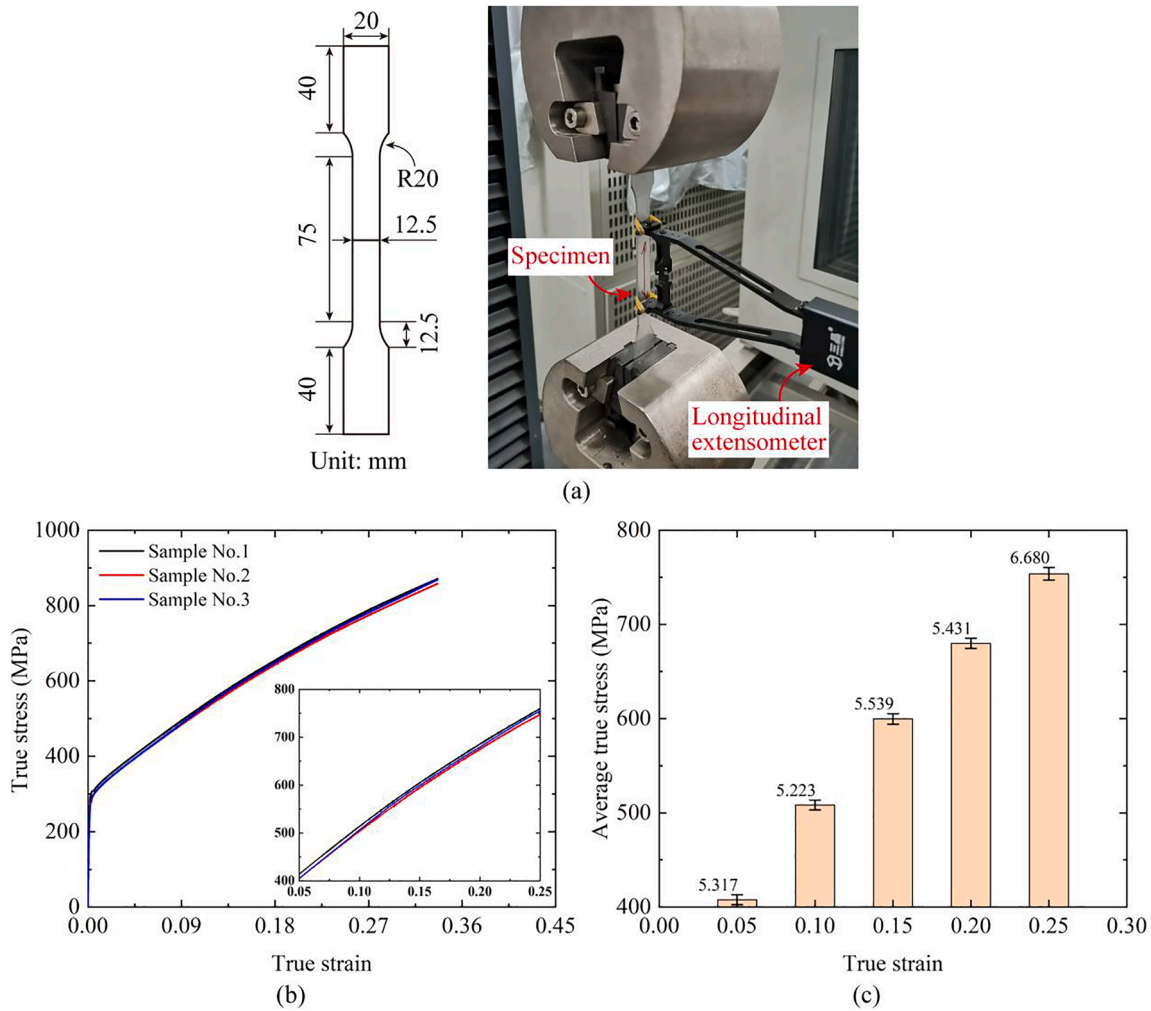


Fig. 5. Quasi-static uniaxial tensile test for AISI 316L steel: (a) geometry of test specimen and experimental set-up, (b) true stress versus true strain curves, and (c) error bars (standard deviations for true stresses measured at selected true strains).

Table 4

Material properties and Johnson-Cook model parameters for AISI 316L steel [58,60] and 40Cr [61].

Material parameter	Notation		Numerical value	
			AISI 316L	40Cr
Young's modulus	$E$	(GPa)	190	210
Poisson ratio	$\nu$		0.3	0.35
Density	$\rho$	(kg/m <sup>3</sup> )	7900	7890
Plasticity model parameters	$A$	(MPa)	244.78	878
	$B$	(MPa)	1324.89	717
	$n$		0.702	0.5
	$C$		0.0124	0.01
	$\dot{\epsilon}_0$		0.001	/
	$m$		0.91	/
	$T_r$	(K)	298	/
	$T_m$	(K)	1504	/
Fracture model parameters	$D_1$		1.06	/
	$D_2$		0.99	/
	$D_3$		0.95	/
	$D_4$		0	/
	$D_5$		0	/

deflection to the mesh sizes of structural and Eulerian elements. Firstly, for Test M-3, the target plate is meshed in plane with varying sizes (i.e., 4.0, 5.0, 7.5, 10 and 20 mm), with three elements used along its thickness direction, while the Eulerian region is meshed with elements having

20 mm edge length. Fig. 6a presents the simulated mid-span deflection versus time curves, which remain almost unchanged as the mesh size is decreased. Further refinements with smaller mesh sizes do not significantly improve the accuracy of calculations, but rather result in considerably increased computational time. To achieve a balance between calculation cost and accuracy, the in-plane mesh size of 5.0 mm is selected for target plates in all subsequent FE simulations.

Next, mesh convergence is examined for the Eulerian domain. Note that the element size chosen for the Eulerian domain is significantly larger than that for the Lagrangian domain, so as to avoid the numerical phenomenon of material leaking [62]. It is also worth noticing that size mismatch between the Lagrangian and Eulerian elements may result in the Eulerian material passing through the Lagrangian domain. In the present study, five mesh sizes (i.e., 15, 20, 25, 30, and 35 mm) are tested for the Eulerian domain and no leakage is found in the simulations. Fig. 6b displays the permanent mid-span deflection versus time curves. It is seen that the difference in simulation results obtained with mesh sizes of 15, 20 and 25 mm is not obvious. Thus, the mesh size of 20 mm is adopted for the Eulerian domain.

Similarly, mesh-sensitive analysis is conducted on sandwich panels. With Test S-2 taken as an example, the permanent mid-span deflection converges as the mesh size is reduced, and the difference in simulation results obtained with mesh sizes of 3.0 and 4.0 mm is not obvious, as shown in Fig. 7a. Thus, for balanced computational cost and numerical accuracy, the overall mesh size of 4.0 mm is used in subsequent simulations. Similarly, for the Eulerian domain, the grid size is determined to

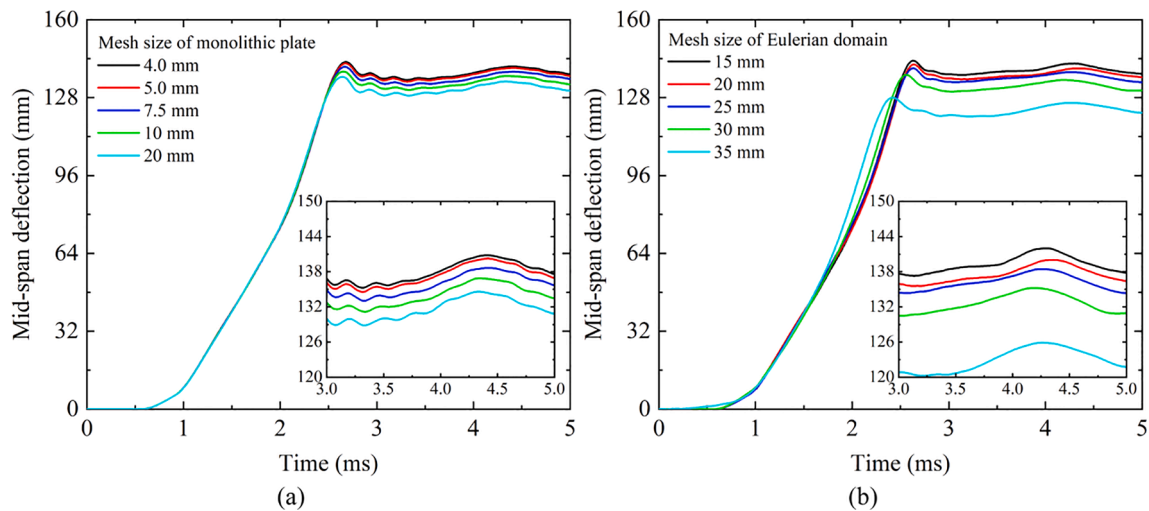


Fig. 6. Mid-span deflection of monolithic plate in Test M-3 versus time curves simulated using (a) varying mesh size for target plate and (b) varying mesh size for Eulerian region.

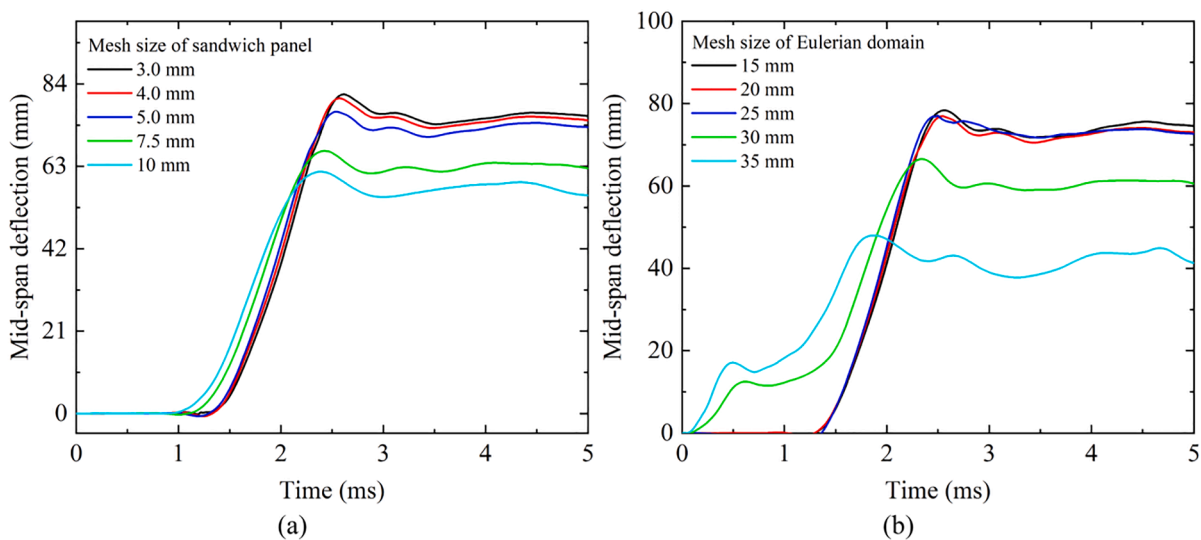


Fig. 7. Mid-span deflection of back face sheet for sandwich panel in Test S-2 versus time curves simulated using (a) varying mesh size for sandwich panel and (b) varying mesh size for Eulerian region.

be 20 mm (Fig. 7b).

## 5. Results and discussion

### 5.1. Experimental results of permanent deformation

#### 5.1.1. Monolithic target plate

Fig. 8 presents the final deformed morphologies of monolithic target plates subjected to internal blast loading from TNT charge at 1 m standoff distance, i.e., Tests M-1 and M-3. The target plate is made of AISI 316L steel in Test M-1, while that in Test M-3 is made of L907A marine steel. The spherical charge has a mass of 0.27 kg (diameter 73.5 mm) in Test M-1 and 1.0 kg (diameter 108.4 mm) in Test M-3; Table 1.

In both tests, large out-of-plane plastic deformation (outward bulging) of target plate occurs, but no fracture is observed. Distinctive plastic hinge lines are found at the edges and diagonals of each target plate, causing it to exhibit an approximately pyramidal shape after the test. The outward bulging in the central region is similar to the shape of spherical charge. These experimental observations are consistent with those reported in previous studies [22,63]. In addition, the “pulling-in

effect” is observed in the clamping regime, where the bolt holes are pulled with slight plastic deformation in-plane, which is similar to that found in free air blast [64]. Such pulling-in effect is known to increase the out-of-plane deflection of a monolithic target plate. The larger in-plane tension force in the boundary region than the clamping force results in movement of the clamped target plate.

#### 5.1.2. Sandwich panel

For Test S-2 selected as representative in this subsection, Fig. 9 presents the final deformed morphology of the all-metallic sandwich specimen, i.e., S-2-A, before and after it is disassembled from the rectangular blast chamber, while Fig. 10 presents corresponding results obtained from post-mortem analysis of the specimen.

Fig. 9a displays the final deformed morphology of sandwich specimen S-2-A. Similar to its monolithic counterpart, the entire deformation mode of the sandwich is dominated by large plastic deformation without any structural damage, with plastic hinge lines appearing on the diagonal of its back face sheet. No significant cracking occurs in welded joints, indicating the high quality of specimen fabrication in the present study. After complete disassembly, the deformed front/back face sheets

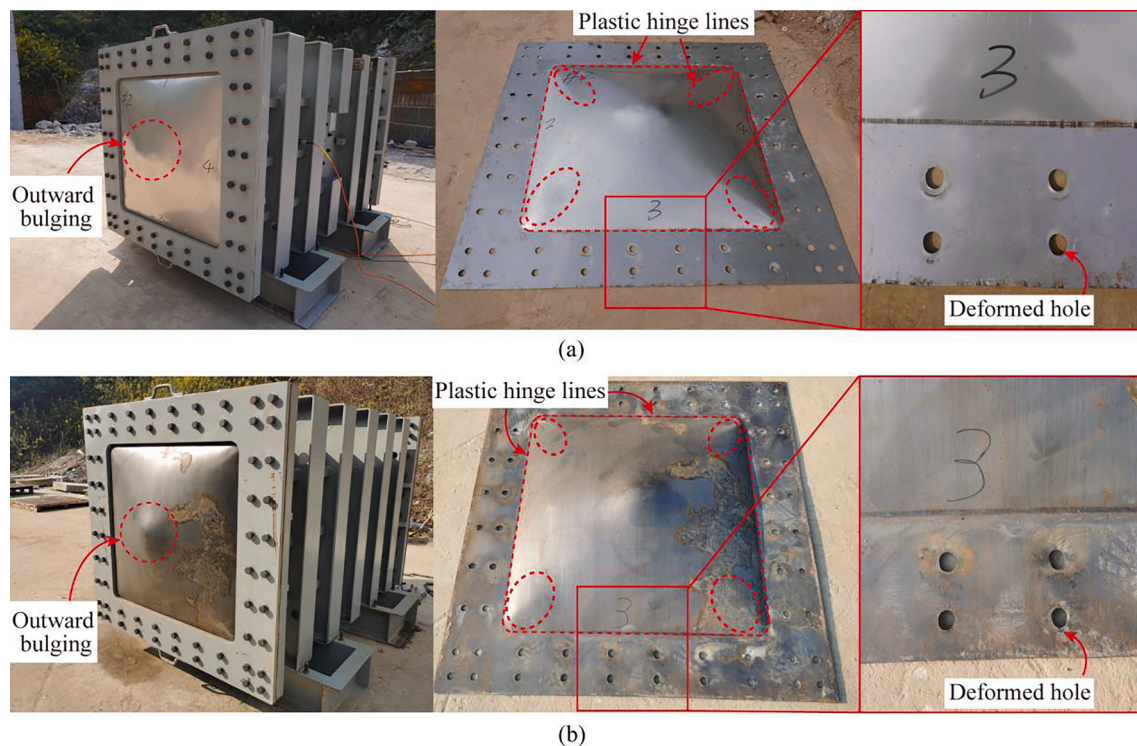


Fig. 8. Final deformed morphologies of monolithic target plates in (a) Test M-1 and (b) Test M-3, with bulging, plastic hinge lines, and deformed bolts holes marked.

and honeycomb core are shown in Fig. 9b, 9c and 10. As the blast wave from charge detonation is transmitted to the clamped sandwich at the end of blast chamber, plastic hinges are formed around its clamped edges and then move diagonally toward the central region. Upon completing the fully confined blast test, stationary plastic hinge lines remain on both the front and back faces, as marked on Fig. 9b and 9c. It should be pointed out that, under fully confined blast loading, both the front and back face sheets experience global bending and stretching. Interestingly, the middlemost unit cell located in the central region of back face sheet exhibits similar deformation modes to the back face as a whole (Fig. 9c), for the size of unit cell in square honeycomb is relatively large in this study. Besides, the bolt holes on the front face sheet exhibit the pulling-in effect, while those on the back face sheet are almost undeformed.

Consider next the deformation of honeycomb core. To this end, the deformed sandwich panel is cut using waterjet along the red dotted line drawn on it to better observe key features of its cross-sectional morphology (Fig. 10a). As shown in Fig. 10b, while symmetrical core deformation occurs, the core webs experience significant plastic buckling especially in the central region. As a result, the maximum compression (7.5 mm) of core web occurs at mid-span, which represents approximately 10 % reduction compared to its original height (75.5 mm). To explore further the deformation mechanisms, two typical core webs taken from the ① and ② regions, shown schematically in Fig. 10c, are analyzed. In region ①, the deformation of honeycomb core web involves multiple folds induced by severe shear straining, as shown in Fig. 10d. In sharp contrast, in the middlemost unit cell where shear straining is not as severe, the buckling of core web exhibits only a single fold, as shown in Fig. 10e.

## 5.2. Validation of FE model

In this section, the accuracy of FE simulated dynamic responses under fully confined blast loading is checked against experimental measurements, mainly from three aspects: internal pressure, permanent mid-span deflection, and deformation mode.

### 5.2.1. Internal pressure

Tests M-1 and S-2 of Table 1 are selected as representatives to validate the accuracy of numerically simulated internal pressure, since the two tests contain the minima and maxima of explosive mass used in the present experimental program, respectively. The simulated internal pressure versus time histories are presented in Fig. 11a for Test M-1 and in Fig. 11b for Test S-2. The results demonstrate that fully confined blast loading from explosive detonation exhibits two different phases, encompassing the shock-wave phase (i.e., reflected blast loading) and the quasi-static phase. The former consists of initial peak pressure and subsequent short-duration reflected waves having attenuated amplitudes. Following the shock wave phase is a long-duration (quasi-static) phase with lower load amplitude. Note that, in a well-enclosed test chamber, the quasi-static pressure is related to the volume of the chamber and the explosion characteristics.

In addition to FE simulations, the two distinct phases are also captured via pressure transducers mounted at positions P1, P2, and P3 on the side walls of blast chamber (Fig. 3), as described in detail in Section 3. In the field tests, the initial peak pressure is recorded by gauge P3 and the quasi-static pressures are recorded using gauges P1 and P2. In Fig. 11 (areas marked in gray), the experimentally measured initial peak pressures and quasi-static pressures are compared with the simulation results. Further comparison between experimentally measured and numerically calculated magnitudes of initial peak pressure and quasi-static pressure is presented in Table 5. For both Tests M-1 and S-2, overall agreement is achieved between experimental and simulation results of initial peak pressure and quasi-static pressure, not only the magnitudes but also the variation trends. Nonetheless, compared with those measured experimentally by gauges P3, i.e., 8.75 MPa and 24.60 MPa for Tests M-1 and S-2, respectively, the simulated initial peak pressures of 10.46 MPa and 28.56 MPa are somewhat higher (Table 5). It should be mentioned that, during the tests, the pressure transducer P3 is affected by a variety of interference factors, such as stress waves propagating through the blast chamber, chamber vibration, and temperature effects. This is likely the reason why the measured initial peak pressure is lower than that numerically calculated. In

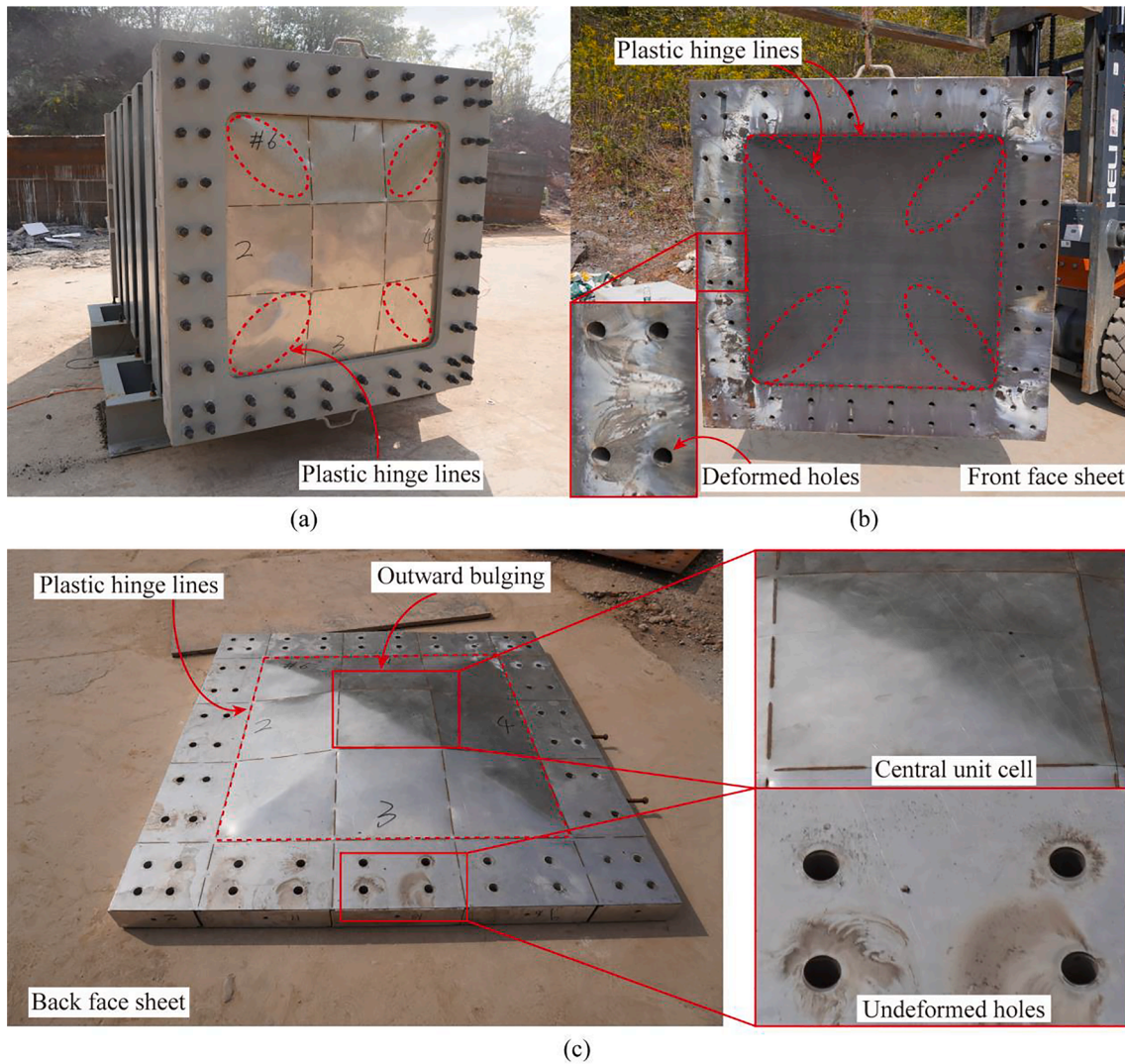


**Fig. 9.** Final deformed morphology of front and back face sheets in Test S-2: (a) before disassembly from rectangular blast chamber with marked plastic hinge lines, (b) front face sheet after disassembly with enlarged view of deformed bolt holes, and (c) back face sheet after disassembly with enlarged view of its central region and undeformed bolt holes.

contrast, the gauges P1 and P2 could in general record the same quasi-static pressure, for it is independent of gauge position. Indeed, the results of Fig. 11 and Table 5 reveal that the quasi-static phase of blast loading measured by gauge P1 agrees excellently well with that measured by P2.

Overall, the proposed FE model successfully captures the main characteristics of fully confined blast loading observed during experimental testing.

### 5.2.2. Permanent mid-span deflection

The validated FE model is employed to simulate all internal blast tests listed in Table 1 such that the permanent deflections of monolithic/sandwich specimens in each test can be calculated. For monolithic target plates tested in first three tests (i.e., test group M), the predicted permanent mid-span deflections ( $\delta_{sim}$ ) are tabulated in Table 6 along with the corresponding measured values ( $\delta_{exp}$ ). For test group S where sandwich panels are tested together with their monolithic counterparts, the numerical and experimental results of permanent mid-span deflections are also listed in Table 6. For each target, the simulated permanent mid-span deflection is estimated from the mid-span deflection versus time curve, which eventually stabilizes as shown in representative Fig. 19c and 19d. Overall, the results demonstrate that the present

FE simulations are able to predict sandwich/monolithic target deflections with reasonable accuracy. The under-prediction for test group M is likely caused by neglecting the after-burning effect in the FE model, while the over-prediction for test group S involving sandwich target is attributed to the fact that air leakage is observed during the blast test, caused likely by intermittent laser welding used in specimen fabrication, gaps between aluminum blocks at boundary regions, etc.

### 5.2.3. Deformation modes

In this subsection, the experimentally observed final deformation modes of target plates are compared with those numerically simulated in Figs. 12 and 13 for Tests M-3 and S-2, respectively. For Test M-3, the simulated deformation mode of monolithic plate (Fig. 12) is in good agreement with that observed in experiment; even the simulated pull-in effect is consistent with that measured (Fig. 8b). Similarly, for the sandwich panel in Test S-2 (Fig. 13), the final deformation mode - including locally folded core webs and plastic hinge lines formed along both the diagonals and welding joints between face sheet and honeycomb core - agree well with those experimentally observed. Moreover, details of the simulated final deformation around bolt holes are displayed in Fig. 14. The equivalent plastic strain around bolt holes on the front face is seen to be greater than that on the back face, which causes

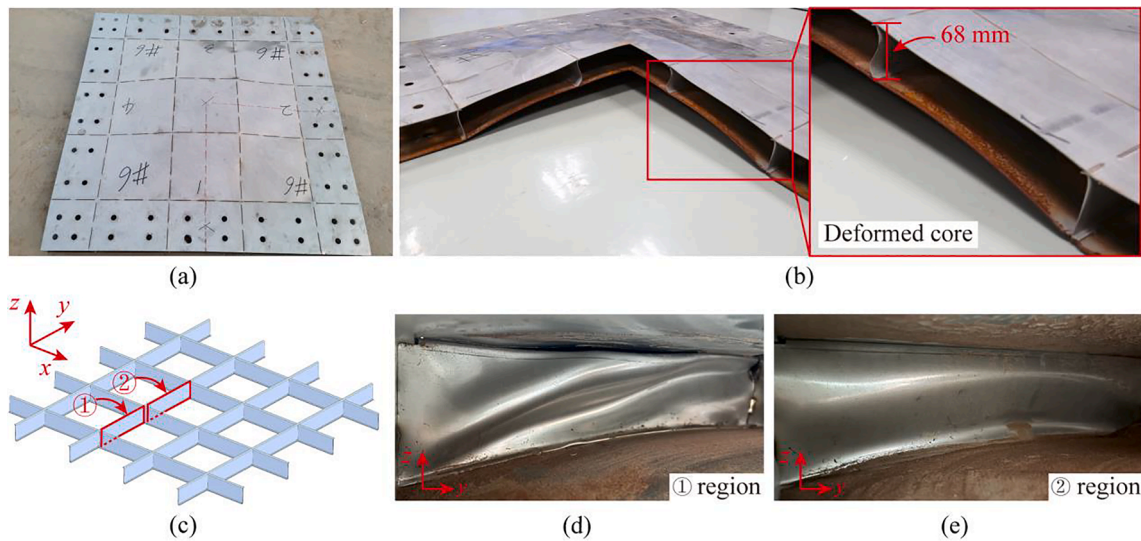


Fig. 10. Final deformed morphology of square honeycomb core in Test S-2: (a) schematic of the red dotted line used for waterjet, (b) cross-sectional view of deformed core with compression of core web in its middlemost cell marked, (c) schematic of square honeycomb core with regions ① and ② marked for further analysis, (d) deformation of core web in region ①, and (e) deformation of core web in region ②.

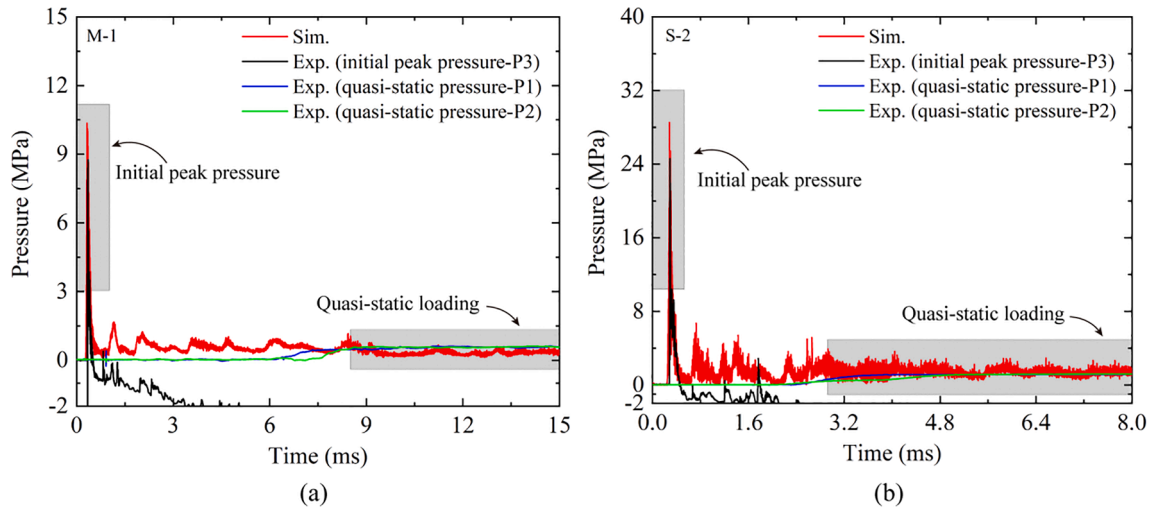


Fig. 11. Comparison between numerically simulated and experimentally measured initial peak and quasi-static pressures for (a) Test M-1 and (b) Test S-2.

Table 5 Comparison between numerically simulated and experimentally measured quasi-static and initial peak pressure values.

Tests	Quasi-static pressure (MPa)				Initial peak pressure (MPa)	
	P1		P2		P3	
	Sim.	Exp.	Sim.	Exp.	Sim.	Exp.
M-1	0.51	0.58	0.51	0.61	10.46	8.75
S-2	1.42	1.11	1.42	1.08	28.56	24.60

visible pull-in effect that is consistent with experimental observation in Fig. 9.

These additional validations not only demonstrate the viability of material constitutive models but also the reliability of FE simulation in the present study.

### 5.3. Blast wave process and structural dynamic response

For each test considered, the dynamic deformation responses of

Table 6 Fully confined blast tests: comparison between experimental measurements and FE simulation results.

Test	Specimen	$\delta_{exp}$ (mm)	$\delta_{sim}$ (mm)	Error (%)
M-1	M-1-A	133.50	120.00	10.11
	M-1-B	138.50	120.00	13.36
	*Avg.	= 136.00	120.00	11.76
M-2	M-2-A	122.50	115.85	5.43
	M-2-B	28.25	26.50	6.19
M-3	M-3-A	150.50	137.25	8.80
	M-3-B	146.80	137.25	6.51
	*Avg.	= 148.65	137.25	7.67
S-1	S-1-A	54.30	56.95	4.88
	S-1-B	27.50	29.50	7.27
S-2	S-2-A	68.50	73.25	6.93
	S-2-B	124.50	133.55	7.27

\*Avg. means averaged value.

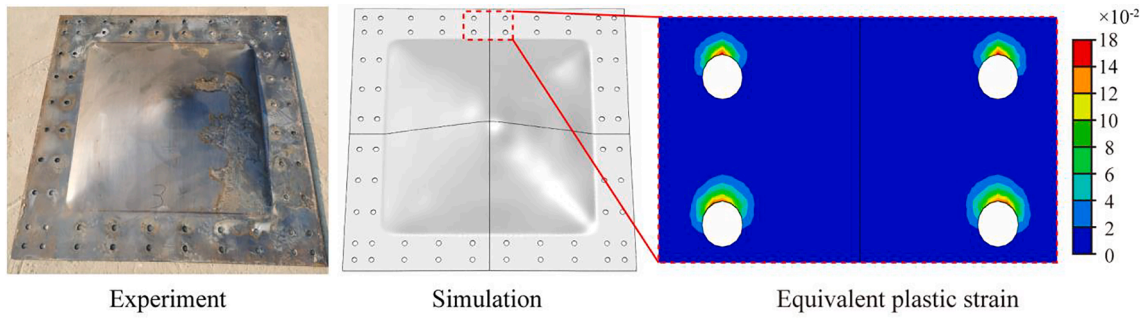


Fig. 12. Comparison between experimentally observed and numerically simulated final deformation modes for clamped monolithic plate under fully confined blast loading (Test M-3).

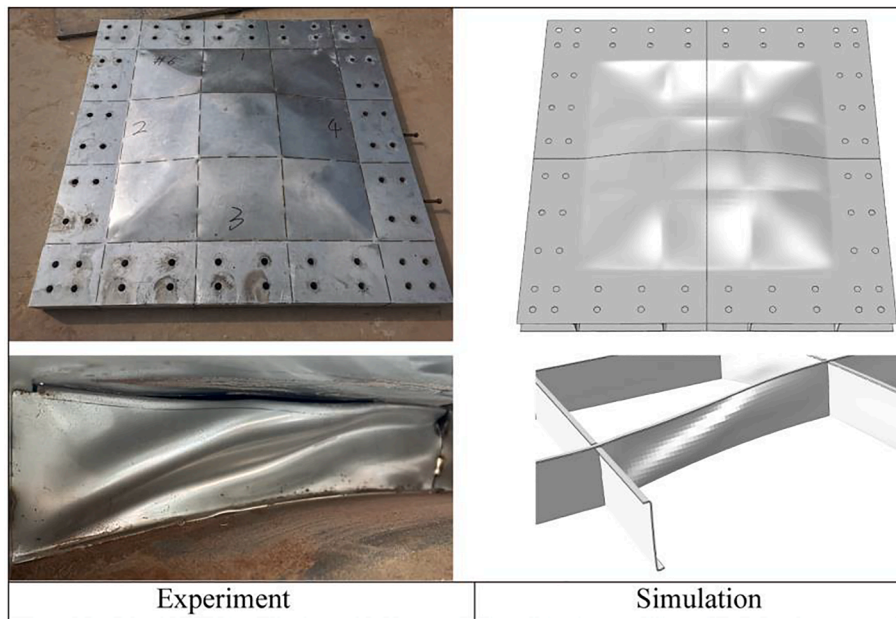


Fig. 13. Comparison between global/local deformation modes observed experimentally and simulated numerically for clamped honeycomb sandwich panel under fully confined blast loading (Test S-2).

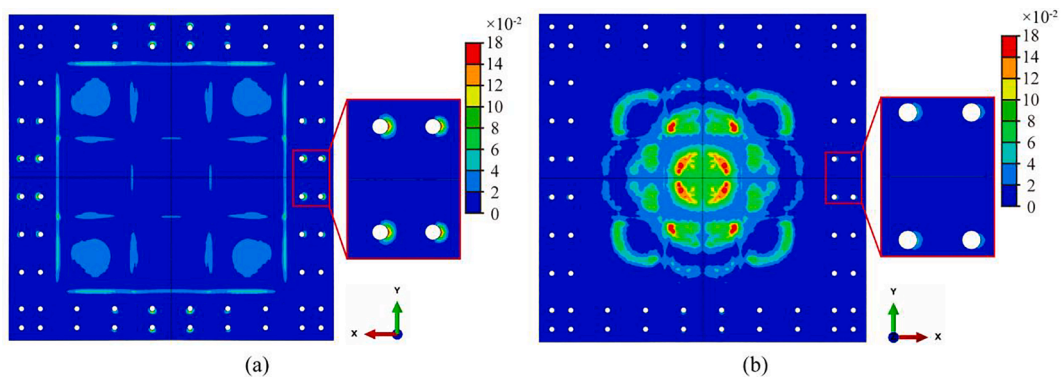


Fig. 14. Details of simulated final deformation around bolt holes on (a) front face and (b) back face of clamped honeycomb sandwich panel under fully confined blast loading (Test S-2). Color legend represents equivalent plastic strain.

target plates clamped at the ends of blast chamber are determined by the propagation and distribution of blast loading acting on them. Thus, upon detonation of spherical TNT explosive, the progressive evolutions of internal pressure field in the blast chamber are presented in this section, with Test M-3 and Test S-2 selected as examples to separately investigate fluid–structure interactions between blast wave and target plate.

5.3.1. Monolithic plate as target

For illustration, Fig. 15 displays the numerically predicted field of air pressure for Test M-3. Note that, for the present calculation, the value of air pressure needs to be added to the atmospheric pressure (0.101957 MPa) due to the EOS model of air. For Test M-3, as the standoff distances between target plates and TNT charge are equal, i.e.,  $R_1 = R_2 = 1$  m, the

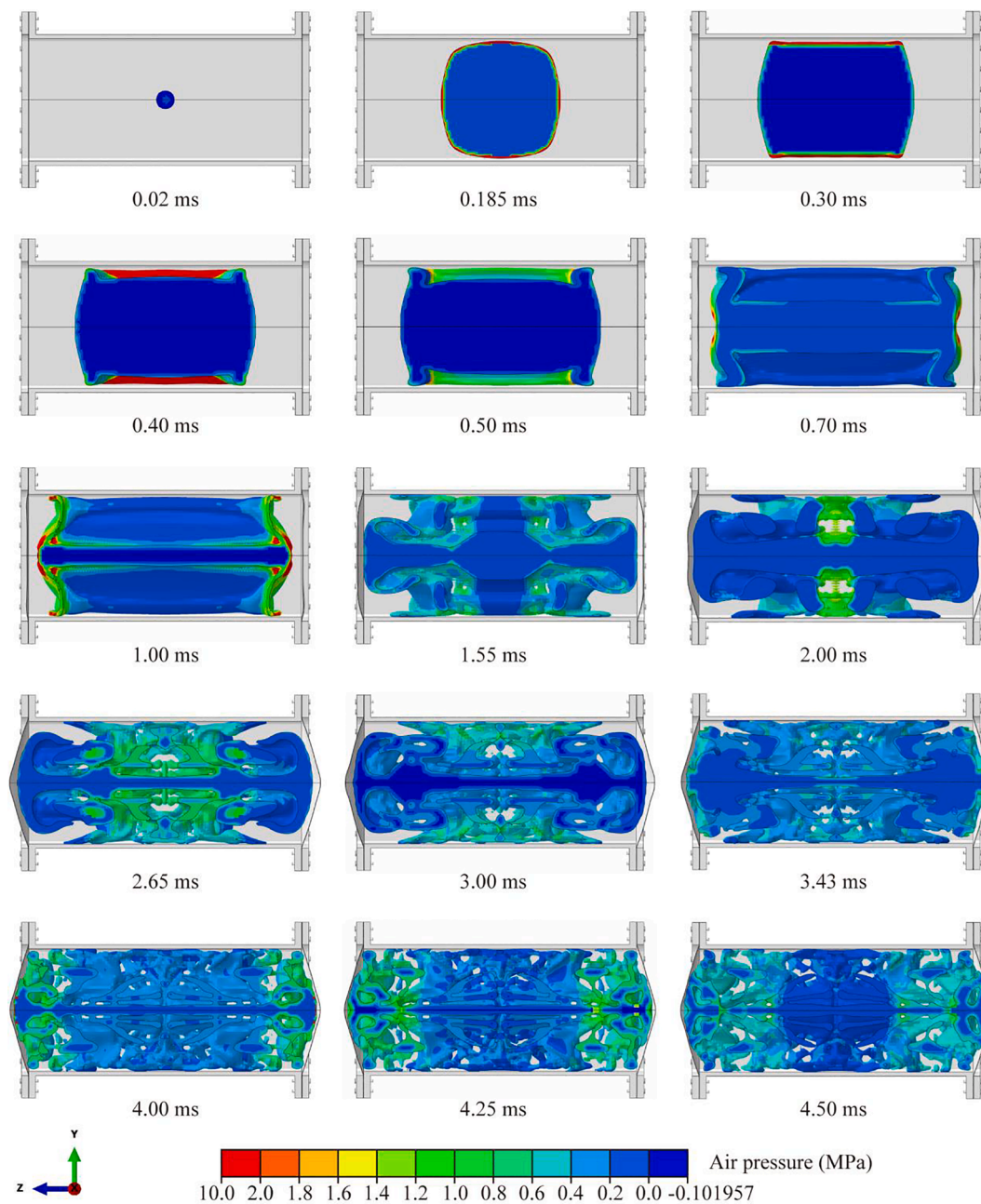


Fig. 15. Evolution of numerically calculated air pressure field at selected times for Test M-3.

profile of pressure wave is symmetrical in magnitude and shape. Further, as the two monolithic target plates are identical, it suffices to consider the dynamic responses of one target, for example, specimen M-3-A clamped at the left end of blast chamber (Table 1).

The results of Fig. 15 reveal that the process of blast wave propagation and reflection can be roughly divided into the following stages. The first stage is before the blast wave propagates to the target plate, with  $t = 0.02 \sim 0.50$  ms. Upon TNT charge detonation at  $t = 0$ , the blast shock wave begins to propagate and, at about  $t = 0.185$  ms, first reaches the top/bottom walls of rectangular blast chamber. Subsequently, reflected shock waves from the rigid top/bottom boundaries are formed at  $t = 0.30 \sim 0.40$  ms. Due to the confinement effect of chamber, the reverberation of blast wave continues to expand towards target plates clamped at both ends of the chamber. The second stage commences when the shock wave first strikes the target and is rapidly reflected. At  $t = 0.70$  ms, the wave converges at the corners of blast chamber with high

pressure and begins to interact with each target. Subsequently, during  $t = 1.0 \sim 2.0$  ms, reflected shock waves form rapidly at each end of chamber and propagate towards the opposite target, converging at the center of chamber at  $t = 2.0$  ms. Meanwhile, each target plate is evidently deformed, first from the corners due to the converging of shock waves. Evolution of the deformation profile of M-3-A target plate across its mid-line along the y-direction is presented in Fig. 16a, where a schematic drawing of the mid-line (dashed line) is shown. Correspondingly, Fig. 16b displays the sequence of target deformation (along the mid-line) at selected times, showing that the deformation initiated at the clamped edges gradually moves towards the central region ( $t = 1.0 \sim 2.0$  ms). Note that the region where the target exhibits zero deflection is exactly its edges clamped via the inserted aluminum blocks and M22 bolts.

After  $t = 2.0$  ms, the reverberating shock waves that converge in the central begin of blast chamber continue to propagate and move towards

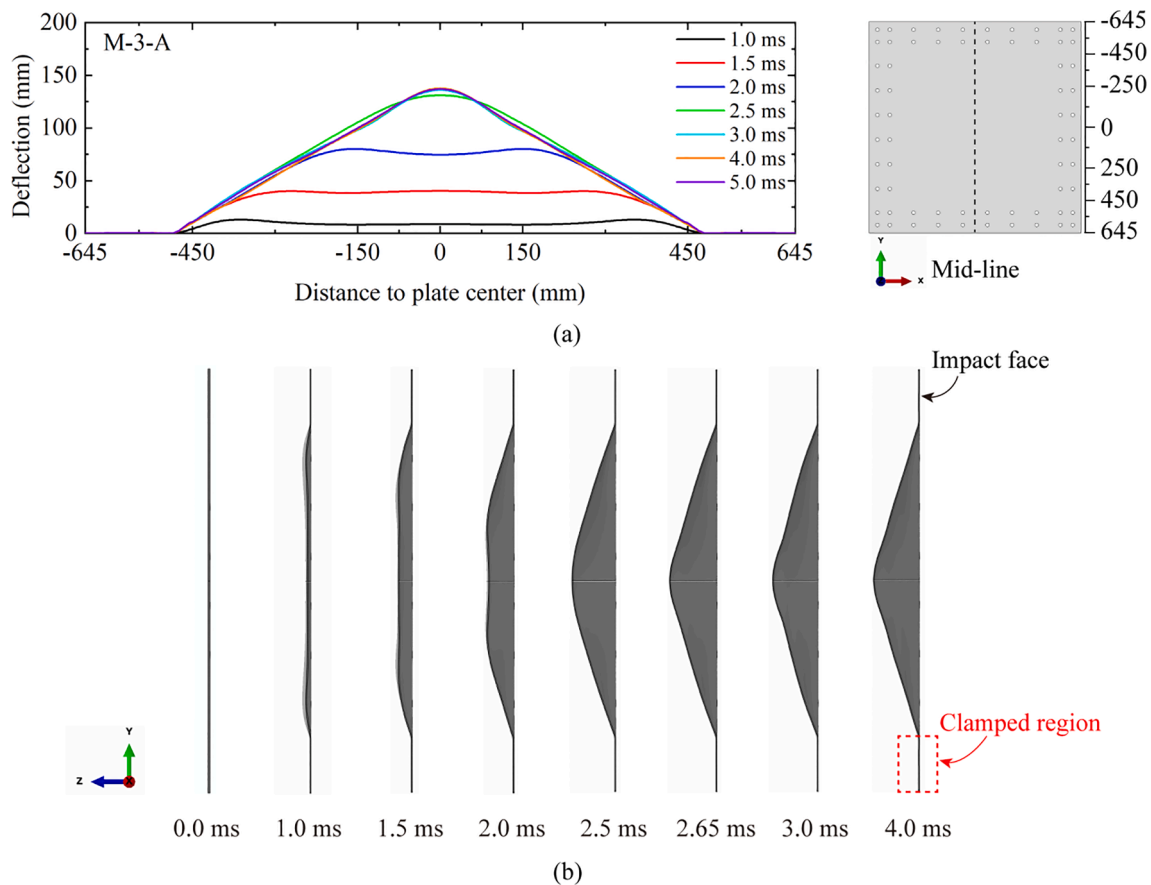


Fig. 16. Dynamic deformation responses of monolithic target plate in Test M-3: (a) deformation profile across mid-line (dashed line) of target plate at selected times after charge detonation, (b) evolution of deformed cross-sectional profile at selected times after charge detonation.

the target plate clamped at each end. Until  $t = 3.43$  ms, the shock waves completely reach the target plate, thus initiating the secondary reflection process. During this stage, the transient deformation of monolithic target plate exhibits outward bulging in its central region ( $t = 2.5$  ms), with the maximum deflection (at plate center) reached at  $t = 2.65$  ms (Fig. 16). Thereafter, the overall profile of target plate remains approximately stable. Subsequently, after the blast wave collides with the target, secondary reflected shock waves again propagate towards the opposite target clamped at the other end ( $t = 3.43 \sim 5$  ms). In other words, at this stage, each target has been loaded by two consecutive reflected shock waves. Nonetheless, the initial reflected wave contributes most to the deformation of target plate, for its deformed profile remains almost constant as it interacts with the secondary reflected wave.

### 5.3.2. Sandwich panel as target

Next, the validated FE model is employed to simulate the dynamic performance of honeycomb sandwich panel (i.e., specimen S-2-A in Test S-2) under fully confined blast loading. Fig. 17 presents the predicted evolution of air pressure field, which is largely similar to that shown in Fig. 15 for Test M-3, and hence is not explained below for brevity.

For both the front and back face sheets, Fig. 18 presents the deformation profile along the mid-line at selected times after detonation. For the front face sheet, the deformation profile exhibits three bumps during  $t = 1.0 \sim 2.0$  ms, corresponding to three square honeycomb cells underneath it. At  $t = 1.0$  ms, the bumps at the edges of the mid-line profile are more pronounced than that in its center, which is contributed to the converging of blast waves at the corners of blast chamber as shown in Fig. 17. The bump in the central area then deforms with increasingly higher velocity and, at  $t = 2.0$  ms, an overall flattened bulging along the

mid-line is formed due to the formation of plastic hinge lines. This is coincident with the period during which the first blast wave interacts with the sandwich panel and completes its reflection (Fig. 17). Subsequently, the overall deformation profile stabilizes except in the central area, where the deformation first increases and then decreases ( $t = 2.0 \sim 5.0$  ms): more in-depth analysis regarding this phenomenon is presented later.

It is interesting to note that the deformation of back face sheet at  $t = 1.0$  ms initially occurs at a distance 150 mm from its center, where the web of honeycomb core is located. Inward bulging in the central region ( $-150$  mm  $\sim$  150 mm) is evident at  $t = 1.5$  ms, which is in contrast to the above-mentioned deformation profile of the front face sheet. The flattened deformation profile in the central region occurs at  $t = 2$  ms, which rapidly transforms into outward bulging, the latter maximized at  $t = 2.5$  ms. Subsequently ( $t = 2.5 \sim 5.0$  ms), the variation of deformation profile is insignificant. The maximum deflection first decreases, then increases, and finally stabilizes, due mainly to the interaction between secondary reflected blast wave and sandwich panel (Fig. 17).

To gain further insight into the phenomena discussed above, the numerically simulated dynamic response of sandwich panel is analyzed. When subjected to unconfined blast loading, the deformation process of a fully clamped sandwich panel exhibits approximately-three sequential phases [28,29,65]. Phase I: transfer of impulse to front face; Phase II: core compression; Phase III: overall bending and stretching. Under fully confined blast loading, as shown in Fig. 19a for Test S-2, the honeycomb sandwich panel exhibits essentially the same deformation processes. However, due to the relatively large cell size of the present sandwich construction, new deformation modes occur locally in each phase, as illustrated below.

Consider first the clamped sandwich panel as a whole. In Phase I, the

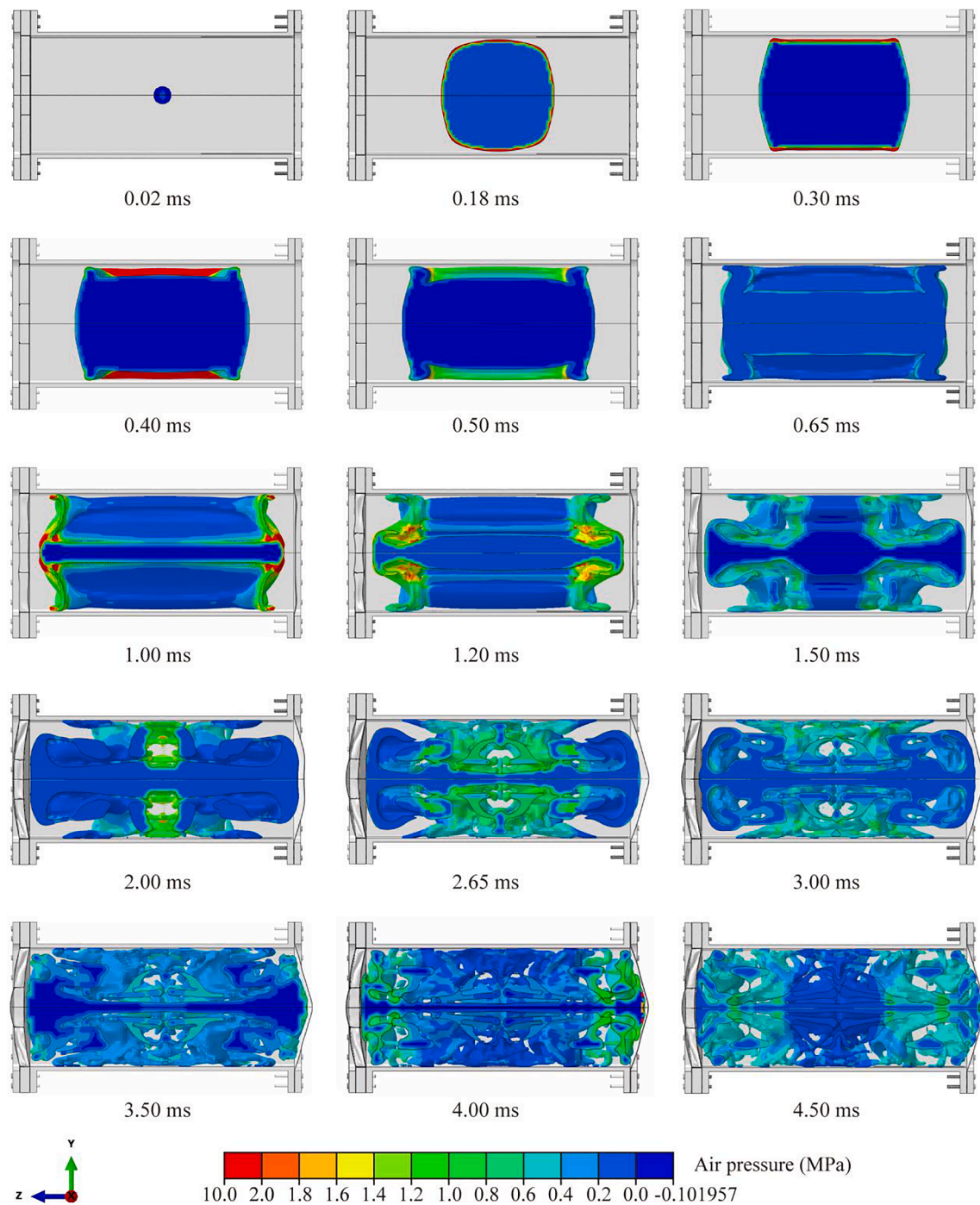


Fig. 17. Evolution of numerically calculated air pressure field at selected times for Test S-2.

blast impulse arrives at the front face ( $t = 0.8$  ms) to form three locally deformed regions due to the presence (and constraint) of honeycomb core underneath it. In Phase II, the honeycomb core receives the impulse transmitted by the front face and begins to compress ( $t = 1.1$  ms). Meanwhile, the back face remains stationary, which is why inward bulging (Fig. 18b) occurs in its central region till  $t = 1.5$  ms. In Phase III, the back face starts to deform (as shown for  $t = 1.8$  ms), causing relative movement between the clamping region and the central region of sandwich panel. As a result, significant shear damage to the core close to the clamped edge occurs, leading to the deformation modes presented in Fig. 10d. Subsequently, at  $t = 2.0$  ms, the entire sandwich panel (except for its clamped edges) acquires roughly a common velocity and is, eventually, brought to rest as the blast energy is dissipated via plastic

bending and stretching.

Consider next local deformation in the central region of the sandwich. Bulged deformation of its back face is observed at  $t = 2.5$  ms. To explore physical mechanisms leading to this behavior, the simulated mid-span displacement and velocity are plotted in Fig. 19b and 19c as functions of time after charge detonation, for both the front and back faces. In Phase I, the sandwich structure as a whole is stationary except for its front face whose velocity gradually increases to a maximum. In Phase II, the front face moves down with a gradually reducing velocity due to the resistance via core compression, while the back face remains stationary. In sharp contrast, in Phase III, the back face deforms with a significantly increasing velocity, which is higher than that of front face during  $t = 1.5 \sim 2.5$  ms. Thereafter ( $t > 2.5$  ms), the mid-span velocity of

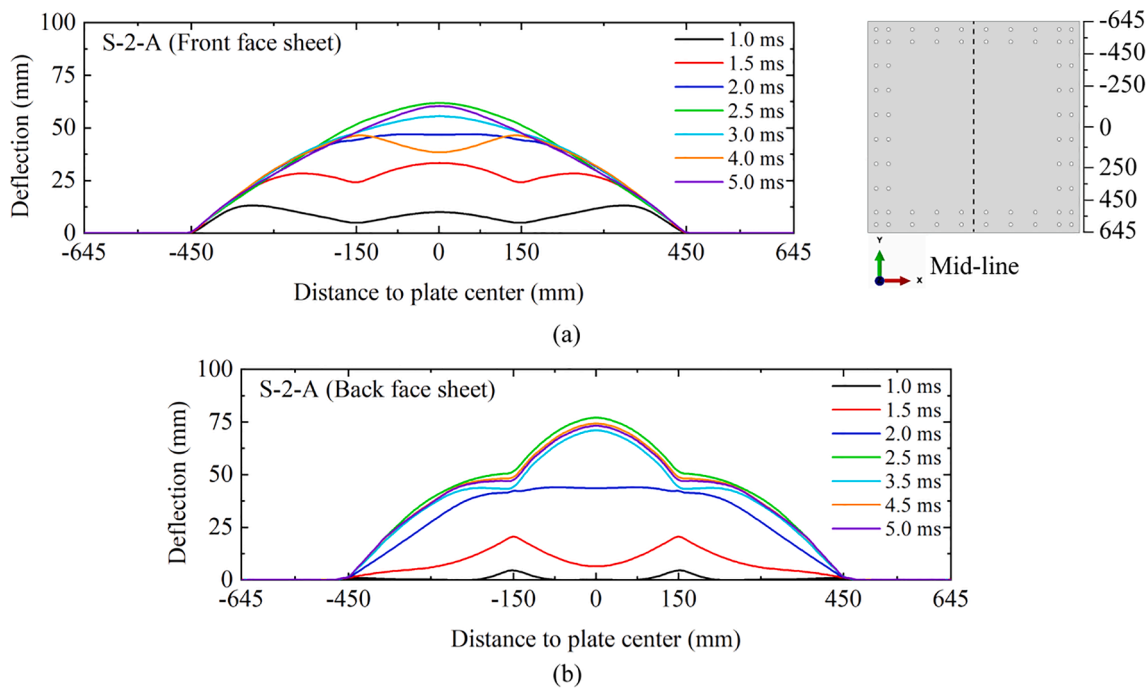


Fig. 18. Numerically predicted deformation profiles across mid-line of (a) front face sheet and (b) back face sheet of sandwich panel at selected times in Test S-2.

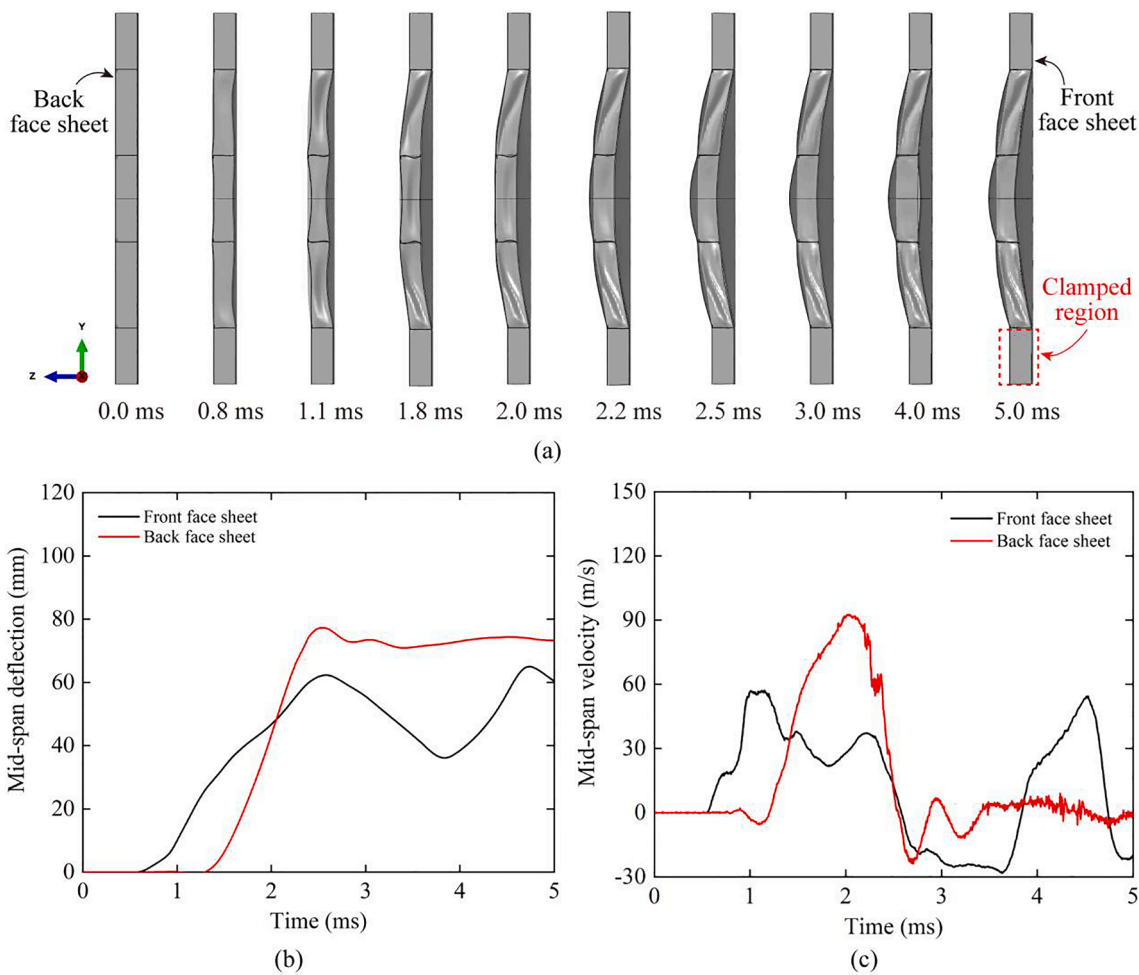


Fig. 19. Numerically simulated dynamic responses of clamped sandwich panel with honeycomb core in Test S-2: (a) evolution of cross-sectional deformation profile, (b) mid-span displacement plotted as a function of time for front and back faces, and (c) mid-span velocity plotted as a function of time for front/back faces.

back face fluctuates within a small scale around zero, while its mid-span deflection becomes stabilized. In comparison, during this stage, the front face experiences elastic oscillation after peak deflection, resulting in large fluctuations (from trough to peak) in its mid-span velocity and deflection.

#### 5.4. Impulse analysis

From the above analyses, we provide a physical explanation for structural transient response based upon the measured/predicted evolution of internal air pressure field. Either the monolithic or sandwich target plate is loaded by two consecutive blast waves, the former formed from explosive detonation (defined as the initial blast wave) and the second formed by reflection from the opposite target (defined as the reflected blast wave). The FE simulation results (Fig. 15 and Fig. 17) reveal that the deformation response of the target is hardly affected by reflected blast wave. To gain insight into the relationship between blast loading and structural response, the impact impulse transferred by blast wave to target is analyzed below.

Again, take Test S-2 as example. Fig. 20a displays the evolution of average contact pressure  $P$  acting on the exposed area of sandwich target plate clamped at one end of blast chamber, caused by its interaction with blast wave. Similar average contact pressure acting on its monolithic counterpart is also presented. For both target plates, the contact pressure exhibits two distinct peaks, corresponding separately to the moment when the initial blast wave and the reflected blast wave interact with the target. The first peak is higher than the second, since the internal pressure weakens with time. Notably, the two target plates exhibit approximately the same contact pressure history, for the set-up of the present fully confined blast tests ensures the symmetry of both initial

and secondary pressure waves. Next, the transmitted impulse per unit area  $I$  of target calculated by integrating the contact pressure with duration is presented in Fig. 20b. The transmitted impulse increases gradually during the early stage of pressure wave interaction and then increases sharply due to the arrival of secondary blast wave.

The results of  $P$  and  $I$  versus time histories as well as the mid-span deflection versus time history of back face are displayed in Fig. 20c for clamped sandwich panel (Test S-2). For comparison, Fig. 20d presents similar results for clamped monolithic plate. For both target types, the mid-span deflection reaches a maximum and then remains relatively constant, indicating that the duration of explosion is longer than the structural response time. The impulse transmitted during the early stage of blast is responsible for the permanent deflection of each target, after which the impulse further increases, but no longer contributes to structural deformation. The reflected blast wave arrives later than the earliest moment when the mid-span deflection reaches stability, which also means that the impulse caused by reflected blast wave has no effect on permanent deflection. The above is known as the phenomenon of impulse saturation [66–68], i.e., not all transmitted impulse causes structural deformation. The present results demonstrate that impulse saturation also occurs in clamped sandwich panel subjected to long-duration fully confined blast.

#### 5.5. Comparison between sandwich and monolithic target plates

In this section, the performance of sandwich panel in terms of mid-span deflection is compared with that of its monolithic counterpart at the same standoff distance, i.e., Test S-2 where the TNT charge (1 kg) is placed at the center of blast chamber (Table 1). Given that the areal mass of sandwich panel  $ism \approx 42.6 \text{ kg/m}^2$ , the equivalent monolithic plate

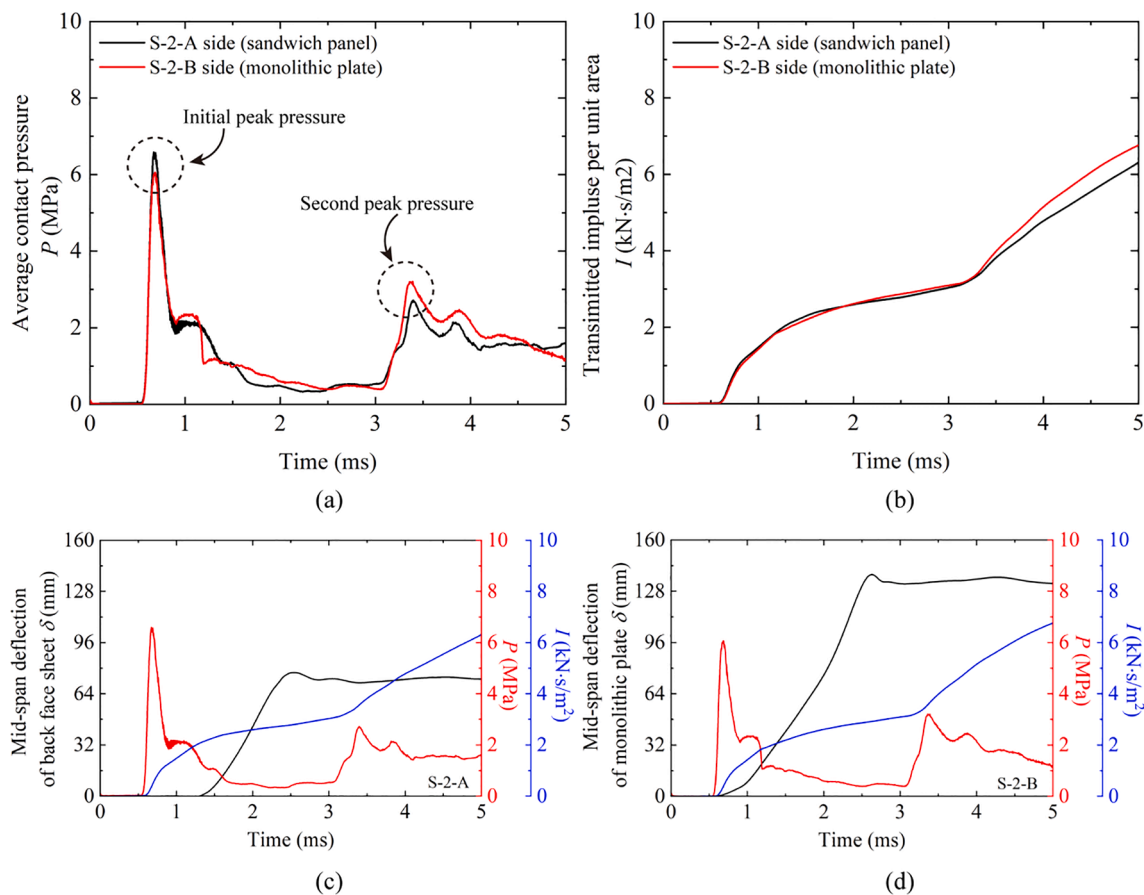


Fig. 20. Evolution of average contact pressure  $P$  (a) and transmitted impulse  $I$  (b) for sandwich/monolithic targets in Test S-2. Evolution of  $P$ ,  $I$ , and permanent mid-span deflection for (c) sandwich panel and (d) monolithic plate in Test S-2.

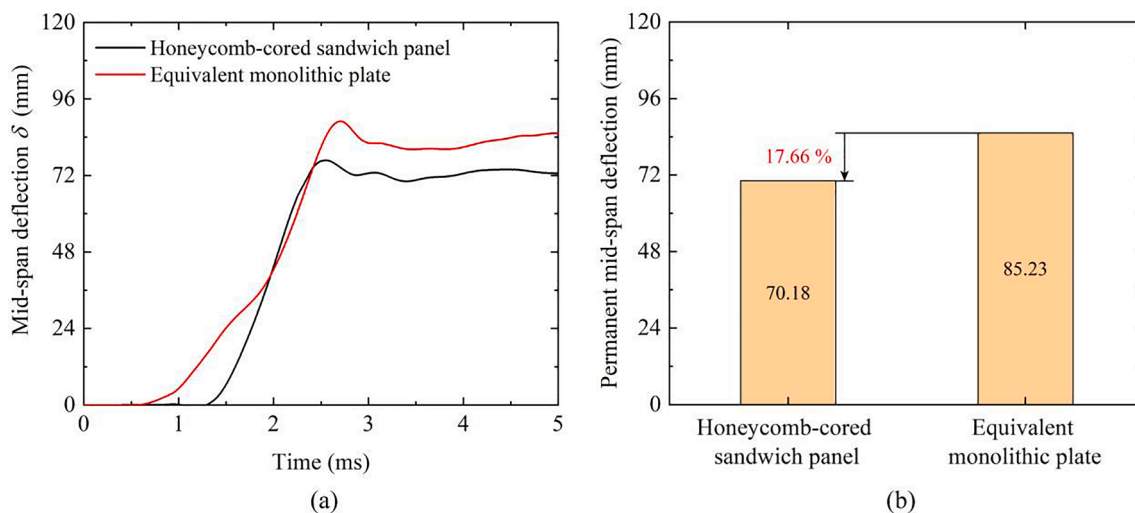


Fig. 21. Comparison between sandwich panel and equivalent monolithic plate under identical confined blast condition: (a) evolution of mid-span deflection, and (b) permanent mid-span deflection.

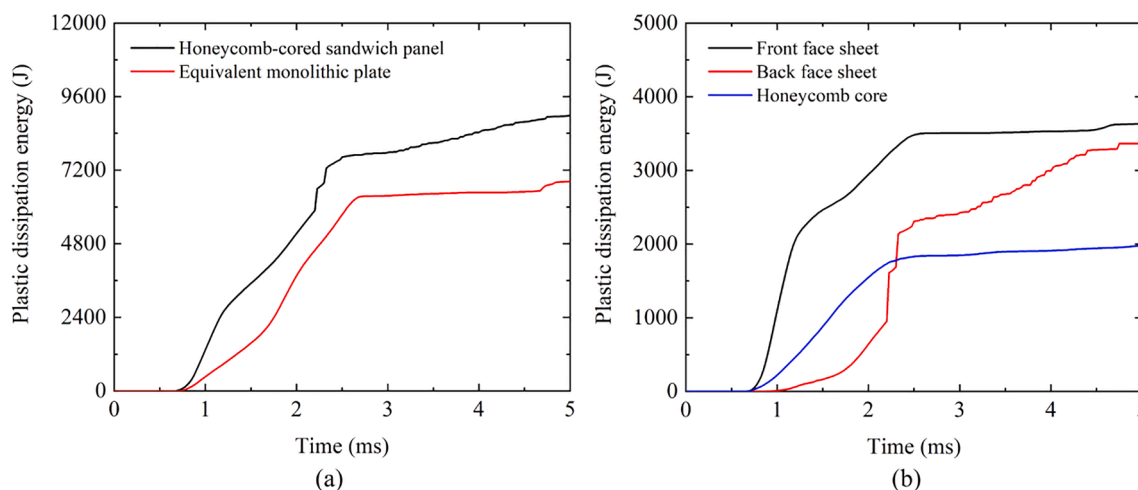


Fig. 22. (a) Comparison of plastic dissipation energy between sandwich panel and equivalent monolithic plate, and (b) plastic dissipation energy of each component for sandwich panel.

has a thickness of  $t_s \approx 5.4$  mm. Fig. 21a compares the numerically calculated evolution of back face mid-span deflection of sandwich panel with that of its monolithic counterpart. The results demonstrate that the honeycomb sandwich panel outperforms the monolithic plate of equal mass. For the case considered, the permanent mid-span deflection of the back face is 70.18 mm, which is 17.66 % smaller than that (85.23 mm) of the monolithic plate, as shown in Fig. 21b. Further, it can be seen from Fig. 22a that the plastic dissipation energy of sandwich panel is larger than that of its monolithic counterpart. As for the constituents of the sandwich, the front face dissipates more plastic energy than others, as shown in Fig. 22b.

It should be pointed out that only preliminary results are presented in this study. Although it is demonstrated that the proposed sandwich panel with square honeycomb core is superior to its monolithic counterpart of equal mass, additional investigation is needed to explore how key geometrical parameters and core topologies would affect the dynamic response of sandwich construction under fully confined blast loading and optimize the configuration for further enhancement in blast/impact resistance.

## 6. Conclusions

A combined experimental and numerical study has been carried out to evaluate, for the first time, how an all-metallic honeycomb sandwich panel would perform under fully confined blast loading in comparison with its monolithic counterpart of equal areal mass density. Ultralight sandwich panels with square honeycomb cores are fabricated and tested in a purposely designed rectangular blast chamber. Internal blast loadings at varying levels are produced from spherical-shaped TNT charge detonation at fixed standoff distance. High-fidelity finite element (FE) modeling with ABAQUS/Explicit is subsequently carried out, with the Coupled-Eulerian-Lagrangian (CEL) method employed to realize the coupling between shock wave and target structure. Good agreement is achieved between numerical predictions and experimental results. Main conclusions drawn are summarized as follows:

- (1) The pressure versus time histories of internal shock loadings on fully-clamped sandwich/monolithic target plates, measured with pressure transducers, are featured by multiple reflected overpressures and a long-duration quasi-static phase with considerably lower pressure amplitude. Under such shock loadings, the sandwich panel suffers global bending/stretching and localized

core compression/shear, while its monolithic counterpart experiences significant large out-of-plane plastic deformation.

- (2) The 3D FE simulations reveal that both the sandwich and monolithic targets are loaded by two consecutive reflected shock waves. The initial reflected wave makes the main contribution to target deformation, for the deflection profile of either sandwich or monolithic target remains almost unchanged during its interaction with the secondary reflected wave.
- (3) The honeycomb sandwich panel exhibits a superior shock resistance to its monolithic counterpart of equal mass, with a 17.66 % reduction in mid-span permanent deflection. Further reduction is expected when the sandwich construction is optimized.

Results of this study provide valuable insight into physical mechanisms leading to the superior performance of sandwich construction under fully confined blast loading, helpful for designing novel lightweight protection structures with enhanced blast resistance for ship construction. Future experimental work with improved testing tools is needed such that detonation-induced air field inside the blast chamber can be accurately measured, thus enabling further validation of numerical simulation results.

#### CRedit authorship contribution statement

**Xue Li:** Data curation, Methodology, Software, Validation, Writing – original draft, Writing – review & editing. **Rui Kang:** Investigation, Visualization, Software. **Cong Li:** Resources. **Zhiyang Zhang:** Investigation. **Zhenyu Zhao:** Project administration, Writing – review & editing, Supervision. **Tian Jian Lu:** Conceptualization, Writing – review & editing, Supervision, Funding acquisition.

#### Declaration of Competing Interest

The authors declare that they have no known competing financial interests or personal relationships that could have appeared to influence the work reported in this paper.

#### Data availability

Data will be made available on request.

#### Acknowledgments

This work was supported by the National Natural Science Foundation of China (12032010, 11902155), by the Natural Science Foundation of Jiangsu Province (BK20190382), by the Research Fund of State Key Laboratory of Mechanics and Control of Mechanical Structures (Grant No. MCMS-I-0222K01), by the Fund of Prospective Layout of Scientific Research for NUAU, and by the Postgraduate Research & Practice Innovation Program of Jiangsu Province (KYCX21\_0178).

#### References

- [1] Geretto C, Chung Kim Yuen S, Nurick GN. An experimental study of the effects of degrees of confinement on the response of square mild steel plates subjected to blast loading. *Int J Impact Eng* 2015;79:32–44. <https://doi.org/10.1016/j.ijimpeng.2014.08.002>.
- [2] Hu Y, Wu C, Lukaszewicz M, Dragos J, Ren J, Haskett M. Characteristics of confined blast loading in unvented structures. *Int J Protective Struct* 2011;2:21–44. <https://doi.org/10.1260/2041-4196.2.1.21>.
- [3] Edri I, Savir Z, Feldgun VR, Karinski YS, Yankelevsky DZ. On Blast Pressure Analysis Due to a Partially Confined Explosion : I. Experimental Studies. *Int J Protective Struct* 2011;2:1–20. <https://doi.org/10.1260/2041-4196.2.1.1>.
- [4] Dragos J, Wu C, Oehlers DJ. Simplification of fully confined blasts for structural response analysis. *Eng Struct* 2013;56:312–26. <https://doi.org/10.1016/j.engstruct.2013.05.018>.
- [5] Salvado FC, Tavares AJ, Teixeira-Dias F, Cardoso JB. Confined explosions: The effect of compartment geometry. *J Loss Prev Process Ind* 2017;48:126–44. <https://doi.org/10.1016/j.jlp.2017.04.013>.
- [6] Silvestrini M, Genova B, Leon Trujillo FJ. Energy concentration factor. A simple concept for the prediction of blast propagation in partially confined geometries. *J Loss Prevention Process Ind* 2009;22:449–54. <https://doi.org/10.1016/j.jlp.2009.02.018>.
- [7] Feldgun VR, Karinski YS, Edri I, Yankelevsky DZ. Prediction of the quasi-static pressure in confined and partially confined explosions and its application to blast response simulation of flexible structures. *Int J Impact Eng* 2016;90:46–60. <https://doi.org/10.1016/j.ijimpeng.2015.12.001>.
- [8] Feldgun VR, Karinski YS, Yankelevsky DZ. A simplified model with lumped parameters for explosion venting simulation. *Int J Impact Eng* 2011;38:964–75. <https://doi.org/10.1016/j.ijimpeng.2011.08.004>.
- [9] Wu C, Lukaszewicz M, Schebella K, Antanovskii L. Experimental and numerical investigation of confined explosion in a blast chamber. *J Loss Prev Process Ind* 2013;26:737–50. <https://doi.org/10.1016/j.jlp.2013.02.001>.
- [10] Qin Y, Wang Y, Wang Z, Yao X. Investigation on similarity laws of cabin structure for the material distortion correction under internal blast loading. *Thin-Walled Struct* 2022;177:109371. <https://doi.org/10.1016/j.tws.2022.109371>.
- [11] Kong XS, Wu WG, Li J, Chen P, Liu F. Experimental and numerical investigation on a multi-layer protective structure under the synergistic effect of blast and fragment loadings. *Int J Impact Eng* 2014;65:146–62. <https://doi.org/10.1016/j.ijimpeng.2013.11.009>.
- [12] Yao S, Zhang D, Lu F, Chen X, Zhao P. A combined experimental and numerical investigation on the scaling laws for steel box structures subjected to internal blast loading. *Int J Impact Eng* 2017;102:36–46. <https://doi.org/10.1016/j.ijimpeng.2016.12.003>.
- [13] Yao S, Zhang D, Lu Z, Lin Y, Lu F. Experimental and numerical investigation on the dynamic response of steel chamber under internal blast. *Eng Struct* 2018;168:877–88. <https://doi.org/10.1016/j.engstruct.2018.03.067>.
- [14] Rushton N, Schleyer GK, Clayton AM, Thompson S. Internal explosive loading of steel pipes. *Thin-Walled Struct* 2008;46:870–7. <https://doi.org/10.1016/j.tws.2008.01.027>.
- [15] Dong Q, Li QM, Zheng JY. Interactive mechanisms between the internal blast loading and the dynamic elastic response of spherical containment vessels. *Int J Impact Eng* 2010;37:349–58. <https://doi.org/10.1016/j.ijimpeng.2009.10.004>.
- [16] Zheng J, Hu Y, Ma L, Du Y. Delamination failure of composite containment vessels subjected to internal blast loading. *Compos Struct* 2015;130:29–36. <https://doi.org/10.1016/j.compstruct.2015.04.013>.
- [17] Yuan Y, Zhang C, Xu Y. Influence of standoff distance on the deformation of square steel plates subjected to internal blast loadings. *Thin-Walled Struct* 2021;164:107914. <https://doi.org/10.1016/j.tws.2021.107914>.
- [18] Li Y, Ren X, Zhao T, Xiao D, Liu K, Fang D. Dynamic response of stiffened plate under internal blast: Experimental and numerical investigation. *Mar Struct* 2021;77. <https://doi.org/10.1016/j.marstruct.2021.102957>.
- [19] Li XD, Yin JP, Zhao PD, Zhang L, Xu YX, Wang Q, et al. The effect of stand-off distance on damage to clamped square steel plates under enclosed explosion. *Structures* 2020;25:965–78. <https://doi.org/10.1016/j.istruc.2020.03.066>.
- [20] Chung Kim Yuen S, Nurick GN, Verster W, Jacob N, Vara AR, Balden VH, et al. Deformation of mild steel plates subjected to large-scale explosions. *Int J Impact Eng* 2008;35:684–703. <https://doi.org/10.1016/j.ijimpeng.2008.02.001>.
- [21] UFC-3-340-02. Structures to resist the effect of accidental explosions. US Department of the Army, Navy and Air Force Technical Manual; 2008.
- [22] Zheng C, Kong X shao, Wu W guo, Xu S xi, Guan Z wei. Experimental and numerical studies on the dynamic response of steel plates subjected to confined blast loading. *International Journal of Impact Engineering* 2018; 113: 144-60. <https://doi.org/10.1016/j.ijimpeng.2017.11.013>.
- [23] Zhang C, Tan PJ, Yuan Y. Confined blast loading of steel plates with and without pre-formed holes. *Int J Impact Eng* 2022;104183. <https://doi.org/10.1016/j.ijimpeng.2022.104183>.
- [24] Dharmasena KP, Wadley HNG, Xue Z, Hutchinson JW. Mechanical response of metallic honeycomb sandwich panel structures to high-intensity dynamic loading. *Int J Impact Eng* 2008;35:1063–74. <https://doi.org/10.1016/j.ijimpeng.2007.06.008>.
- [25] Dharmasena KP, Wadley HNG, Williams K, Xue Z, Hutchinson JW. Response of metallic pyramidal lattice core sandwich panels to high intensity impulsive loading in air. *Int J Impact Eng* 2011;38:275–89. <https://doi.org/10.1016/j.ijimpeng.2010.10.002>.
- [26] Wadley HNG, Borvik T, Olovsson L, Wetzel JJ, Dharmasena KP, Hopperstad OS, et al. Deformation and fracture of impulsively loaded sandwich panels. *J Mech Phys Solids* 2013;61:674–99. <https://doi.org/10.1016/j.jmps.2012.07.007>.
- [27] Han B, Qin K, Yu B, Wang B, Zhang Q, Lu TJ. Honeycomb-corrugation hybrid as a novel sandwich core for significantly enhanced compressive performance. *Mater Des* 2016;93:271–82. <https://doi.org/10.1016/j.matdes.2015.12.158>.
- [28] Fleck NA, Deshpande VS. The resistance of clamped sandwich beams to shock loading. *J Appl Mech, Trans ASME* 2004;71:386–401. <https://doi.org/10.1115/1.1629109>.
- [29] Qiu X, Deshpande VS, Fleck NA. Dynamic response of a clamped circular sandwich plate subject to shock loading. *J Appl Mech, Trans ASME* 2004;71:637–45. <https://doi.org/10.1115/1.1778416>.
- [30] Hutchinson JW, Xue Z. Metal sandwich plates optimized for pressure impulses. *Int J Mech Sci* 2005;47:545–69. <https://doi.org/10.1016/j.ijmecsci.2004.10.012>.
- [31] Rathbun HJ, Radford DD, Xue Z, He MY, Yang J, Deshpande V, et al. Performance of metallic honeycomb-core sandwich beams under shock loading. *Int J Solids Struct* 2006;43:1746–63. <https://doi.org/10.1016/j.ijsolstr.2005.06.079>.
- [32] Xue Z, Hutchinson JW. Crush dynamics of square honeycomb sandwich cores. *Int J Numer Meth Eng* 2006;65:2221–45. <https://doi.org/10.1002/nme.1535>.

- [33] Qiu X, Deshpande VS, Fleck NA. Finite element analysis of the dynamic response of clamped sandwich beams subject to shock loading. *Eur J Mech-A/Solids* 2003;22(6):801–14. <https://doi.org/10.1016/j.euromechsol.2003.09.002>.
- [34] Xue Z, Hutchinson JW. A comparative study of impulse-resistant metal sandwich plates. *Int J Impact Eng* 2004;30(10):1283–305. <https://doi.org/10.1016/j.ijimpeng.2003.08.007>.
- [35] McShane GJ, Radford DD, Deshpande VS, et al. The response of clamped sandwich plates with lattice cores subjected to shock loading. *Eur J Mech-A/Solids* 2006;25(2):215–29. <https://doi.org/10.1016/j.euromechsol.2005.08.001>.
- [36] Zhu F, Zhao L, Lu G, et al. Deformation and failure of blast-loaded metallic sandwich panels—experimental investigations. *Int J Impact Eng* 2008;35(8):937–51. <https://doi.org/10.1016/j.ijimpeng.2007.11.003>.
- [37] Zhu F, Zhao L, Lu G, et al. A numerical simulation of the blast impact of square metallic sandwich panels. *Int J Impact Eng* 2009;36(5):687–99. <https://doi.org/10.1016/j.ijimpeng.2008.12.004>.
- [38] Li X, Zhang P, Wang Z, et al. Dynamic behavior of aluminum honeycomb sandwich panels under air blast: Experiment and numerical analysis. *Compos Struct* 2014;108:1001–8. <https://doi.org/10.1016/j.compstruct.2013.10.034>.
- [39] Khan MS, Abdul-Latif A, Koloor SSR, et al. Representative cell analysis for damage-based failure model of polymer hexagonal honeycomb structure under the out-of-plane loadings. *Polymers* 2020;13(1):52. <https://doi.org/10.3390/polym13010052>.
- [40] Khan MS, Koloor SSR, Tamin MN. Effects of cell aspect ratio and relative density on deformation response and failure of honeycomb core structure. *Mater Res Express* 2020;7(1):015332. <https://doi.org/10.1088/2053-1591/ab6926>.
- [41] Russell BP, Liu T, Fleck NA, et al. The soft impact of composite sandwich beams with a square-honeycomb core. *Int J Impact Eng* 2012;48:65–81. <https://doi.org/10.1016/j.ijimpeng.2011.04.007>.
- [42] Ma X, Li X, Li S, et al. Blast response of gradient honeycomb sandwich panels with basalt fiber metal laminates as skins. *Int J Impact Eng* 2019;123:126–39. <https://doi.org/10.1016/j.ijimpeng.2018.10.003>.
- [43] Nayak SK, Singh AK, Belegundu AD, et al. Process for design optimization of honeycomb core sandwich panels for blast load mitigation. *Struct Multidiscip Optim* 2013;47(5):749–63. <https://doi.org/10.1007/s00158-012-0845-x>.
- [44] Sun G, Chen D, Wang H, et al. High-velocity impact behaviour of aluminium honeycomb sandwich panels with different structural configurations. *Int J Impact Eng* 2018;122:119–36. <https://doi.org/10.1016/j.ijimpeng.2018.08.007>.
- [45] Catapano A, Montemurro M. A multi-scale approach for the optimum design of sandwich plates with honeycomb core. Part II: the optimisation strategy. *Compos Struct* 2014;118:677–90. <https://doi.org/10.1016/j.compstruct.2014.07.058>.
- [46] Ebrahimi H, Ghosh R, Mahdi E, et al. Honeycomb sandwich panels subjected to combined shock and projectile impact. *Int J Impact Eng* 2016;95:1–11. <https://doi.org/10.1016/j.ijimpeng.2016.04.009>.
- [47] Ma F, Liang H, Pu Y, et al. Crashworthiness analysis and multi-objective optimization for honeycomb structures under oblique impact loading. *Int J Crashworthiness* 2022;27(4):1128–39. <https://doi.org/10.1080/13588265.2021.1909861>.
- [48] Yu R, Li X, Yue Z, Li A, Zhao Z, Wang X, et al. Stress state sensitivity for plastic flow and ductile fracture of L907A low-alloy marine steel: From tension to shear. *Mater Sci Eng A* 2022;835:142689. <https://doi.org/10.1016/j.msea.2022.142689>.
- [49] Li X, Kang R, Li C, Zhang Z, Zhao Z, et al. Plastic deformation and ductile fracture of L907A ship steel at increasing strain rate and temperature. *J Impact Eng* 2023;174:104515. <https://doi.org/10.1016/j.ijimpeng.2023.104515>.
- [50] Dhib Z, Guermazi N, Gaspérini M, et al. Cladding of low-carbon steel to austenitic stainless steel by hot-roll bonding: microstructure and mechanical properties before and after welding. *Mater Sci Eng A* 2016;656:130–41. <https://doi.org/10.1016/j.msea.2015.12.088>.
- [51] Benson DJ, Okazawa S. Contact in a multi-material Eulerian finite element formulation. *Comput Methods Appl Mech Eng* 2004;193:4277–98. <https://doi.org/10.1016/j.cma.2003.12.061>.
- [52] Benson DJ. Computational methods in Lagrangian and Eulerian hydrocodes. *Comput Methods Appl Mech Eng* 1992;99:235–394. [https://doi.org/10.1016/0045-7825\(92\)90042-1](https://doi.org/10.1016/0045-7825(92)90042-1).
- [53] ABAQUS User Manual, Dassault Systems Simulia Corporation, USA; 2020.
- [54] Lee EL, Hornig HC, Kury JW. *Adiabatic expansion of high explosive detonation products[R]*. Livermore, CA (United States): Univ. of California Radiation Lab. at Livermore; 1968.
- [55] Mousavi AAA, Burley SJ, Al-Hassani STS. Simulation of explosive welding using the Williamsburg equation of state to model low detonation velocity explosives. *Int J Impact Eng* 2005;31(6):719–34. <https://doi.org/10.1016/j.ijimpeng.2004.03.003>.
- [56] Fallon C, McShane GJ. Fluid-structure interactions for the air blast loading of elastomer-coated concrete. *Int J Solids Struct* 2019;168:138–52. <https://doi.org/10.1016/j.ijsolstr.2019.03.017>.
- [57] Johnson, G.R. A constitutive model and data for materials subjected to large strains, high strain rates, and high temperatures. *Proc. 7th Inf. Symp. on Ballistics* 1983; 541–547.
- [58] Li X, Roth CC, Tancogne-Dejean T, Mohr D. Rate- and temperature-dependent plasticity of additively manufactured stainless steel 316L: Characterization, modeling and application to crushing of shell-lattices. *Int J Impact Eng* 2020;145:103671. <https://doi.org/10.1016/j.ijimpeng.2020.103671>.
- [59] Johnson GR, Cook WH. Fracture characteristics of three metals subjected to various strains, strain rates, temperatures and pressures. *Eng Fract Mech* 1985;21(1):31–48. [https://doi.org/10.1016/0013-7944\(85\)90052-9](https://doi.org/10.1016/0013-7944(85)90052-9).
- [60] Bianchetti C, Muñoz DP, Leblé B, Bouchard PO. Ductile failure prediction of piping notched AISI 316L using uncoupled ductile failure criteria. *Int J Press Vessel Pip* 2021;191. <https://doi.org/10.1016/j.ijpvp.2021.104333>.
- [61] Xu W, Wang D. Fatigue / impact analysis and structure – connection – performance integration multi-objective optimization of a bolted carbon fiber reinforced polymer / aluminum assembled wheel. *Compos B* 2022;243:110103. <https://doi.org/10.1016/j.compositesb.2022.110103>.
- [62] Langdon GS, Ozinsky A, Yuen CK, S. The response of partially confined right circular stainless steel cylinders to internal air-blast loading. *Int J Impact Eng* 2014;73:1–14. <https://doi.org/10.1016/j.ijimpeng.2014.05.002>.
- [63] Zhang D, Yao S, Lu F, Song J, Ding Y. Dynamic response and damage analysis of steel box wall under internal blast loading. *Adv Mech Eng* 2019;11:1–11. <https://doi.org/10.1177/1687814018822601>.
- [64] Olson MD, Nurick GN, Fagnan JR. Deformation and rupture of blast loaded square plates-predictions and experiments. *Int J Impact Eng* 1993;13:279–91. [https://doi.org/10.1016/0734-743X\(93\)90097-Q](https://doi.org/10.1016/0734-743X(93)90097-Q).
- [65] Zhu F, Wang Z, Lu G, Nurick G. Some theoretical considerations on the dynamic response of sandwich structures under impulsive loading. *Int J Impact Eng* 2010;37:625–37. <https://doi.org/10.1016/j.ijimpeng.2009.11.003>.
- [66] Zhu L, Yu TX. Saturated impulse for pulse-loaded elastic-plastic square plates. *Int J Solids Struct* 1997;34:1709–18. [https://doi.org/10.1016/S0020-7683\(96\)00111-4](https://doi.org/10.1016/S0020-7683(96)00111-4).
- [67] Zhu L, Bai X, Yu TX. The saturated impulse of fully clamped square plates subjected to linearly decaying pressure pulse. *Int J Impact Eng* 2017;110:198–207. <https://doi.org/10.1016/j.ijimpeng.2016.12.012>.
- [68] Tian LR, Chen FL, Zhu L, Yu TX. Large deformation of square plates under pulse loading by combined saturation analysis and membrane factor methods. *Int J Impact Eng* 2020;140. <https://doi.org/10.1016/j.ijimpeng.2020.103546>.